LAWRENCE
LIVERMORE
NATIONAL
LABORATORY

UCRL-JRNL-222101

Effects of WENO flux reconstruction order and spatial resolution on reshocked two-dimensional Richtmyer-Meshkov instability

M. Latini, O. Schilling, W. Sun Don

June 15, 2006

Journal of Computational Physics

Effects of WENO flux reconstruction order and spatial resolution on reshocked two-dimensional Richtmyer-Meshkov instability

Marco Latini [a] Oleg Schilling [b,*] Wai Sun Don [c]

[a] *Applied and Computational Mathematics, California Institute of Technology, Pasadena, California 91125*

[b] *University of California, Lawrence Livermore National Laboratory, Livermore, California 94551*

[c] *Division of Applied Mathematics, Brown University, Providence, Rhode Island 02912*

Abstract

Weighted essentially non-oscillatory (WENO) simulations of the reshocked two-dimensional single-mode Richtmyer-Meshkov instability using third-, fifth- and ninth-order spatial flux reconstruction and uniform grid resolutions corresponding to 128, 256 and 512 points per initial perturbation wavelength are presented. The dependence of the density, vorticity, simulated density Schlieren and baroclinic production fields, mixing layer width, circulation deposition, mixing profiles, production and mixing fractions, energy spectra, statistics, probability distribution functions, numerical turbulent kinetic energy and enstrophy production/dissipation rates, numerical Reynolds numbers, and numerical viscosity on the order and resolution is investigated to long evolution times. The results are interpreted using the implicit numerical dissipation in the characteristic projection-based, finite-difference WENO method. It is shown that higher order higher resolution simulations have lower numerical dissipation. The sensitivity of the quantities considered to the order and resolution is further amplified following reshock, when the energy deposition by the second shock-interface interaction induces the formation of small-scale structures. Lower-order lower-resolution simulations preserve large-scale structures and flow symmetry to late times, while higher-order higher-resolution simulations exhibit fragmentation of the structures, symmetry breaking and increased mixing. Similar flow features are qualitatively and quantitatively captured by either approximately doubling the order or the resolution. Additionally, the computational scaling shows that increasing the order is more advantageous than increasing the resolution for the flow considered here. The present investigation suggests that the ninth-order WENO method is well-suited for the simulation and analysis of complex multi-scale flows and mixing generated by shock-induced hydrodynamic instabilities.

Preprint submitted to Journal of Computational Physics *9 June 2006*

Key words: Richtmyer-Meshkov instability, weighted essentially non-oscillatory (WENO) method, mixing properties, reshock, numerical dissipation

1 Introduction

The Richtmyer-Meshkov instability is a fundamental fluid instability that develops when perturbations on an interface separating gases with different properties grow following the passage of a shock. This instability is typically studied in shock tube experiments, in which an incident shock passes through an initially perturbed interface separating the gases. Following the passage of the shock, the interface is set in motion along the direction of shock propagation and a transmitted shock enters the second gas. The misalignment of $\boldsymbol{\nabla}\rho$ and $\boldsymbol{\nabla}p$ causes a deposition of vorticity $\boldsymbol{\omega} \equiv \boldsymbol{\nabla} \times \boldsymbol{u}$ on the interface through baroclinic vorticity production $\mathcal{P} \equiv (\boldsymbol{\nabla}\rho \times \boldsymbol{\nabla}p)/\rho^2$: in two dimensions

$$\frac{\mathrm{d}\boldsymbol{\omega}}{\mathrm{d}t} = \mathcal{P} - \boldsymbol{\omega}\,\boldsymbol{\nabla}\cdot\boldsymbol{u}\,, \tag{1}$$

where $\mathrm{d}/\mathrm{d}t \equiv \partial/\partial t + \mathbf{u}\cdot\nabla$ is the convective derivative. The vorticity deposited on the interface by the shock drives the instability, resulting in interpenetrating bubbles and spikes. Complex roll-ups and vorticity with strong cores later form. The transmitted shock reflects from the shock tube end wall and interacts with the evolving interface during *reshock*, further contributing to the appearance of complex interacting fluid and wave structures.

In the present work, the formally high-order accurate weighted essentially non-oscillatory (WENO) shock-capturing method using a third-order total-variation diminishing (TVD) Runge-Kutta time-evolution scheme ([1] and references therein) is applied to the reshocked two-dimensional single-mode Richtmyer-Meshkov instability for long evolution times. The initial conditions and computational domain are modeled [2] after the single-mode, Mach 1.21 air(acetone)/SF_6 shock tube experiment of Collins and Jacobs [3]. As the Richtmyer-Meshkov instability-induced flow contains shock waves, a direct numerical simulation (DNS) is not possible due to the prohibitively small scales needed to resolve the complex interactions of the shock with the density interfaces and the shocks themselves. As a result, numerical investigations of this instability typically utilize conservative Eulerian shock-capturing methods that do not resolve all of the spatial scales and small-scale interactions,

* Corresponding author.
Email addresses: mlatini@acm.caltech.edu (Marco Latini), schilling1@llnl.gov (Oleg Schilling), wsdon@cfm.brown.edu (Wai Sun Don).

but instead ensure that fundamental quantities are conserved across a shock and that the shock speed is accurately captured. As numerical results from such simulations are used to interpret and to better understand the physical mechanisms in the evolution of the Richtmyer-Meshkov instability, it is essential to ascertain how such results depend on the numerical algorithm (e.g., the order of flux reconstruction and resolution in the present study).

This study systematically and self-consistently explores and quantifies the sensitivity of a broad array of quantities characterizing single-mode reshocked Richtmyer-Meshkov instability-induced mixing on the order of WENO flux reconstruction (third, fifth and ninth) and on the grid resolution (128, 256 and 512 points per initial perturbation wavelength). Most of these quantities were previously considered in the description of amplitude growth [2] and of the physics of reshock [4]. Here, the density, vorticity, simulated density Schlieren and baroclinic vorticity production fields are qualitatively compared from the simulations. Also compared are the mixing layer widths, circulation, mixing profiles, production and mixing fractions, energy spectra, statistics, probability distribution functions, numerical turbulent kinetic energy and enstrophy production/dissipation rates, numerical Reynolds numbers and numerical viscosities. As the results were obtained for a two-dimensional Euler flow, the differences in these quantities depend solely on the numerical dissipation and not on molecular dissipation and diffusion, or on physics due to vortex stretching present in three dimensions. Most studies based on the solution of the Euler equations have focused on the numerical 'convergence' of some small set of quantities, such as the perturbation amplitude or mixing layer width in the Rayleigh-Taylor instability [5–7] and Richtmyer-Meshkov instability [8–10], over limited evolution times with respect to grid refinement. The present work is conducted in the spirit of the two-dimensional investigation of double Mach reflection and single-mode Rayleigh-Taylor instability [11], which emphasized the computational advantage of higher order (ninth) WENO schemes over lower order (fifth) schemes for complex flows. The present study is both quantitative and qualitative, and examines to what extent different orders of reconstruction and resolutions capture physical quantities characterizing Richtmyer-Meshkov instability-induced mixing. The WENO method is well-suited for such an investigation, as it is possible to perform simulations identical in every other respect except for the reconstruction order, allowing a self-consistent study distinct from utilizing *entirely different numerical methods* with different formal orders of spatial and temporal accuracy [12].

This paper is organized as follows. The numerical method and the set of simulations of the two-dimensional reshocked Richtmyer-Meshkov instability using different orders of WENO reconstruction and grid resolutions are summarized in Sec. 2, including a discussion of the benefits of formally high-order (high-resolution) methods for investigating complex flows with shocks. The effects of order and resolution on the density, vorticity, simulated density Schlieren

and baroclinic vorticity production fields are discussed in Sec. 3. The effects of order and resolution on the mixing layer width and circulation deposition are discussed in Sec. 4. The effects of order and resolution on the mixing profiles, production and mixing fractions, energy spectra, statistics, and probability distribution functions are discussed in Sec. 5. As the results depend on the intrinsic numerical dissipation, a quantitative estimate of this dissipation is presented in Sec. 6. Finally, conclusions, including a discussion of the relative computational cost of the simulations, are presented in Sec. 7.

2 The WENO method and two-dimensional simulations of reshocked single-mode Richtmyer-Meshkov instability

The WENO reconstruction in the conservative finite-difference shock-capturing method used in the present study is briefly described, and its benefits for investigating complex hydrodynamic flows with shocks are discussed here. In particular, as shown later, formally higher-order reconstructions are less dissipative and have greater resolving power than lower-order ones [13]: this demonstrates that high-order WENO methods are suitable for investigating multi-dimensional shock-driven flows in which the dynamics of a wide range of scales and complex wave structures must be characterized with high fidelity.

2.1 Equations solved and description of the WENO algorithm

In the present simulations, the Euler equations augmented by the mass fraction conservation equation for the second gas (used here to determine the mixing layer width and to quantitatively assess various mixing properties)

$$\frac{\partial \boldsymbol{\phi}}{\partial t} + \frac{\partial \boldsymbol{F}}{\partial x} + \frac{\partial \boldsymbol{G}}{\partial y} = 0 \tag{2}$$

are solved, where the conservative variables, $\boldsymbol{\phi}$, and inviscid fluxes, $\boldsymbol{F}$ and $\boldsymbol{G}$, are

$$\boldsymbol{\phi} = (\rho, \rho\,u, \rho\,v, \rho\,e, \rho\,m)^T \ , \tag{3}$$

$$\boldsymbol{F} = \left(\rho\,u, \rho\,u^2 + p, \rho\,u\,v, (\rho\,e + p)\,u, \rho\,m\,u\right)^T \ , \tag{4}$$

$$\boldsymbol{G} = \left(\rho\,v, \rho\,u\,v, \rho\,v^2 + p, (\rho\,e + p)\,v, \rho\,m\,v\right)^T \ . \tag{5}$$

Here, ρ is the density, $\mathbf{u} = (u, v)$ is the velocity, p is the pressure, $e = (u^2 + v^2)/2 + p/(\gamma - 1)$ is the total energy per unit mass, m is the mass

fraction (here of the denser sulfur hexafluoride gas, SF_6) and $p = \rho RT$ is the ideal gamma law gas pressure (R is the gas constant).

The simulations were performed using the finite-difference WENO shock-capturing method [1]. The eigensystem of fluxes in the Euler equations is obtained from the Jacobian of the Roe-averaged fluxes in each spatial dimension. The eigenvalues and eigenvectors are obtained via the linearized Roe Riemann solver [14]. Lax-Friedrichs flux-splitting is used to split the original fluxes into their positive and negative components (with additional artificial dissipation to obtain smoother fluxes [1]). The positive and negative flux components are then projected in the characteristic fields using the left eigenvectors to form the positive and negative characteristic fields at each cell center. A piecewise-polynomial of degree r is used to reconstruct the projected fluxes at the cell boundaries with high-order of accuracy: a weighted convex combination of all possible rth-degree piecewise-polynomial approximations ($r = 2$, 3 and 5 for third-, fifth- and ninth-order, respectively) of the characteristic fields using the neighboring cell-centered values is constructed and evaluated at the boundaries of a given cell. For a given reconstruction order, there are r possible rth-degree piecewise-polynomials, with properties depending on the smoothness of the underlying solution. As the polynomials may use stencils containing discontinuities (and, thus, induce Gibbs oscillations), a weighted average of all of the possible polynomial reconstructions at a point is computed. The weights of the r possible stencils around a given cell center are computed from the projected flux via a divided difference. Essentially zero weights are assigned to polynomials crossing discontinuities and nearly-equal weights are assigned to polynomials over smooth regions. The *formal* order of accuracy for the derivative of the flux is $2r - 1$ in smooth flow regions. In the present study, the semi-discrete equations are evolved in time using the third-order total variation diminishing (TVD) Runge-Kutta method [1].

The conservative finite-difference discretization of the Euler equations with WENO flux reconstruction contains implicit truncation errors that can be regarded as a nonlinear, adaptive numerical dissipation. The present simulations can be interpreted as a class of *implicit large-eddy simulations* (ILES) [15–18], in which the equations are implicitly filtered by the discretization and the numerical dissipation is a surrogate for a dissipation provided by an explicit subgrid-scale model. As the non-dissipative compressible fluid dynamics equations are formally ill-posed, this numerical dissipation regularizes the method. As a result, quantities obtained from such simulations depend on the resolution and cannot be regarded as fully resolved. ILES methods typically dissipate velocity and scalar fluctuations approximately in the same manner numerically: the numerical Schmidt number is of $O(1)$, which may provide a reasonable model for the mixing of ideal gases. In principle, the reduced numerical dissipation of high-order WENO schemes can be coupled with explicit subgrid-scale models to perform conventional large-eddy simulations.

2.2 Benefits of the WENO method for simulating complex shocked flows

Formally high-order methods better resolve complex flow features at long evolution times than second- and third-order methods. Higher order methods are also more computationally efficient than lower order methods for the same accuracy [19,20]. In particular, sufficiently high order WENO methods are well-suited for the simulation of complex, compressible evolving flows containing shocks and structures having a wide range of scales. For example, the interaction of a shock and a bubble was simulated using the fifth-order finite-difference WENO method with two gammas [21]. The advantage of WENO methods is realized in complex multi-dimensional flows, as demonstrated here for the *reshocked* Richtmyer-Meshkov instability.

Upwinding in the WENO method leads to large numerical dissipation in relatively smooth flow regions away from shocks. This dissipation can be reduced by hybridizing the WENO method with a high-order scheme, and the resolving power can be improved by optimizing the stencil with a compact central-difference scheme in smooth flow regions [22]. Mapped WENO schemes were developed to improve the accuracy at critical points where derivatives vanish [23]. A hybrid fifth-order compact upwind-WENO scheme was developed for shock-turbulence interaction [24]. A hybrid scheme based on the weighted average of a compact scheme [24] and the fifth-order WENO scheme was subsequently developed [25] using a weight function that avoids an abrupt transition from one scheme to the other. High-order accurate, hybrid central-WENO schemes [26,27] and a hybrid spectral-WENO scheme [28] were also recently developed. In the present work, higher-order (ninth-order) WENO reconstruction is used instead to achieve lower numerical dissipation.

The code used presently provides an MPI parallel framework for one-, two- or three-dimensional simulations of the fully-nonlinear evolution of hydrodynamic instabilities and late-time mixing generated by single- or multi-mode Richtmyer-Meshkov and Rayleigh-Taylor instabilities. The ratio of specific heats is constant for both gases in the currently implemented single-gamma algorithm, so that some properties of the flow may not be predicted very accurately (i.e., transmitted and reflected shock speeds, time of reshock, initial interface velocity), but the mixing properties are not expected to be strongly affected by the single-gamma formulation, as the flow is nearly incompressible over most of the evolution for the Mach number considered [29,30].

	Coarse (128)	Medium (256)	Fine (512)
Ninth-order	WENO9C	WENO9M	WENO9F
Fifth-order	WENO5C	WENO5M	WENO5F
Third-order	WENO3C	WENO3M	WENO3F

Table 1
Keys used to denote simulations with different order of WENO flux reconstruction and grid resolution. The number in parentheses is the number of grid points per initial perturbation wavelength λ.

2.3 Simulations of reshocked single-mode Richtmyer-Meshkov instability

Two-dimensional simulations of the reshocked Richtmyer-Meshkov instability modeled after the Mach 1.21 experiment of Collins and Jacobs [2,3] are presented and analyzed in the present work. The simulations are summarized in Table 1, where WENONX indicates the order N = 3, 5 or 9 with optional resolution X = C, M or F (*coarse*, *medium* and *fine* grid resolution, respectively), e.g., WENO5M is the fifth-order WENO method with 256 points per initial perturbation wavelength. *Order* and *resolution* always refer to the order of WENO flux reconstruction and to the spatial grid resolution, respectively. The simulations were run to a late time of 18 ms to determine the effects of the interaction of the reflected rarefaction wave with the layer, and to investigate the late-time decay of the flow. The results presented in a separate study [2,4] were obtained using WENO5M and WENO9M.

The initial conditions for the numerical simulations [2] were adapted from the Mach 1.21 air(acetone)/SF_6 experimental shock tube configuration of Collins and Jacobs [3]. As the current simulations use a single-gamma formulation, the experimental upstream conditions were matched. The adiabatic exponent $\gamma = 1.24815$ corresponding to an air(acetone) mixture was used. The pre-shock Atwood number was $A^- = \left(\rho^-_{SF_6} - \rho^-_{aa}\right)/\left(\rho^-_{SF_6} + \rho^-_{aa}\right) = 0.605$. To match the dimensions of the shock tube test section, the computational domain had streamwise and spanwise length $L_x = 78$ cm and $L_y = 8.9$ cm, respectively, with the centerline of the perturbed initial interface located at $x_s = 3$ cm from the edge of the domain (the physical spanwise domain was 17.8 cm, and symmetry was used in the y-direction). An adaptive domain capability in the code allows the initial domain in x to be much smaller than L_x: the initial value $L_x = 9.3$ cm was chosen in the present simulations. The computational domain in the x direction was elongated in 3 cm increments until a total length of 78 cm was attained. A CFL number of 0.45 was used in all of the simulations. The initial sinusoidal interface $\eta(y) = a_0^- \sin(2\pi y/\lambda)$ had pre-shock amplitude $a_0^- = 0.2$ cm and wavelength $\lambda = 5.9333$ cm. An initial diffusion layer thickness of $\delta = 0.5$ cm was used, where the thickness function

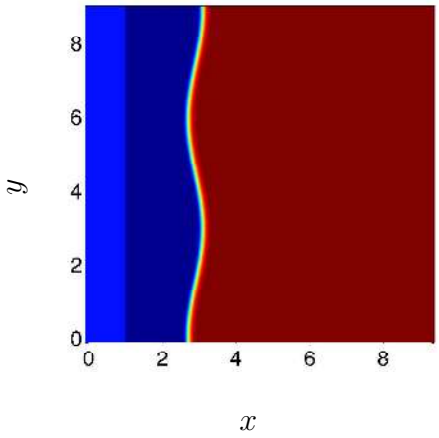

Fig. 1. The incident shock and the initial density field, including the diffuse interface separating the air(acetone) (blue) and the SF_6 (red), obtained using Eq. (6).

(multiplying the density) is

$$S(x,y) = \begin{cases} 1 & d \leq 0 \\ \exp\left(-\alpha \left|d\right|^8\right) & 0 < d < 1 \\ 0 & d \geq 1 \end{cases}, \tag{6}$$

$d = [x_s + \eta(y) + \delta - x]/(2\delta)$, and $\alpha = -\ln\beta$ (β is machine zero). The initial density is shown in Fig. 1.

The following boundary conditions were used: (1) inflow at the test section entrance in the streamwise (x) direction; (2) reflecting at the end wall of the test section in the streamwise direction, and; (3) symmetric in the spanwise (y) direction corresponding to the cross-section of the test section. The reflecting boundary condition is implemented by reversing the normal component of the velocity vector: $u(x,t) = -u(x,t)$ at $x = L_x$ and at the ghost points, which is exact and does not generate spurious noise.

3 The effects of order and resolution on the density, vorticity, simulated density Schlieren and baroclinic vorticity production fields

As the Richtmyer-Meshkov instability develops, bubbles of air(acetone) 'rise' into the SF_6 and spikes of SF_6 'fall' into the air(acetone). Following this initial growth, the spikes form roll-ups that develop the characteristic mushroom shape of the instability. The density and vorticity fields $\rho(x,y)$ and $\omega(x,y)$ at 6 ms are shown in Fig. 2, before the reflected shock from the end wall reshocks the interface. The images were obtained by rotating the density and vorticity fields from the simulations 90° counterclockwise. The spike of SF_6 (red) rolls up and the bubble of air(acetone) (blue) 'rises'. The vorticity shows

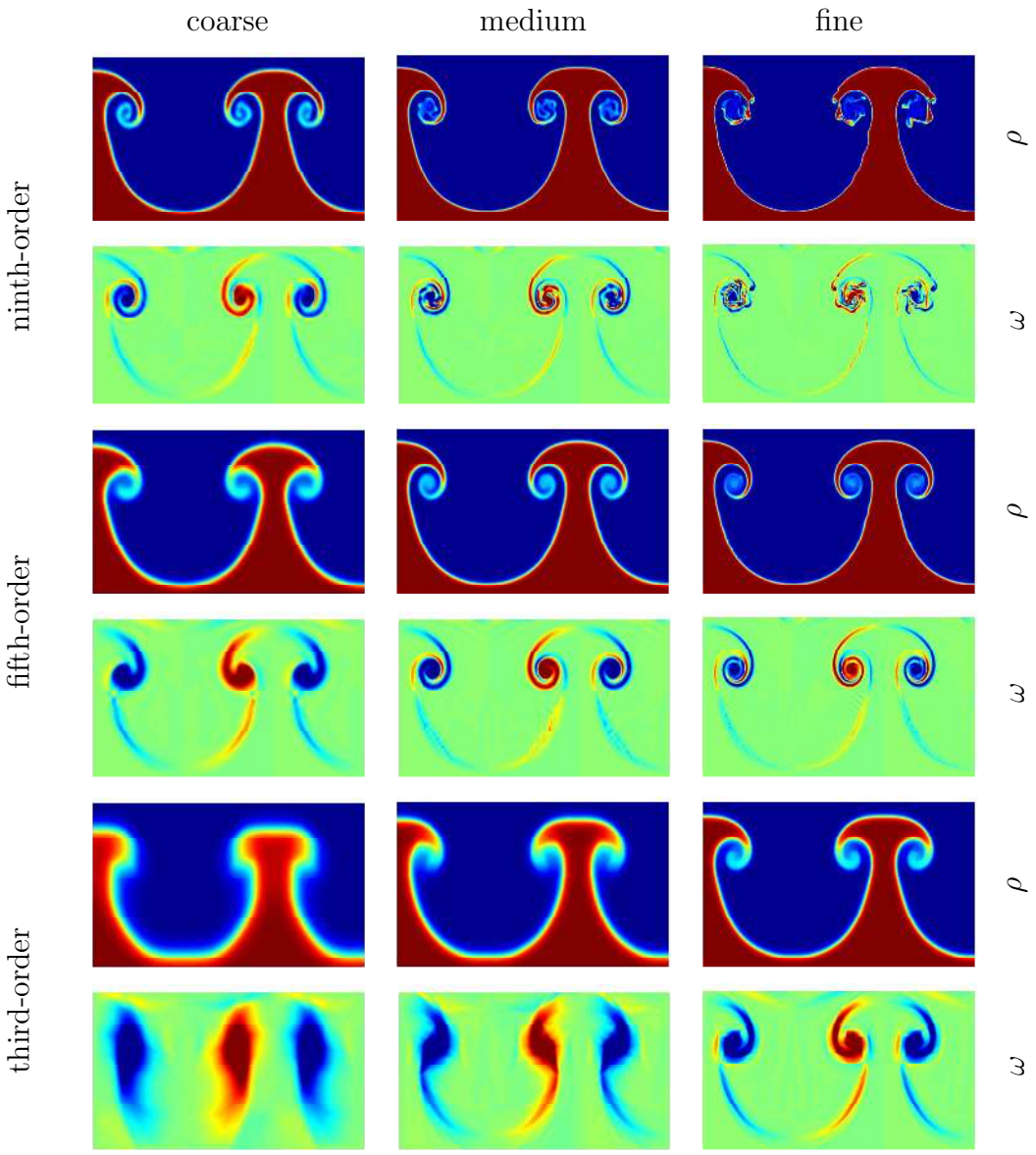

Fig. 2. The density and vorticity fields at 6 ms (before reshock) from the third-, fifth- and ninth-order simulations on the coarse, medium and fine grids.

the strong positive core rotating counter-clockwise (red) and the strong negative core rotating clockwise (blue), corresponding to the centers of the roll-ups. As the order and resolution increase, the roll-up becomes better defined and sharper, smaller-scale features appear within, and the vorticity exhibits more concentrated, smaller cores. The roll-up in the WENO5M, WENO5F and WENO9 simulations contains a vortex bilayer with strong negative vorticity surrounded by a small layer of positive vorticity and vice versa: this bilayer becomes sharper as the order and resolution increase, and additional complex structures form within the roll-up in the WENO9F simulation. Such structures have also been seen in piecewise-parabolic method simulations [31,32], and is apparently a manifestation of a physical process observed in experi-

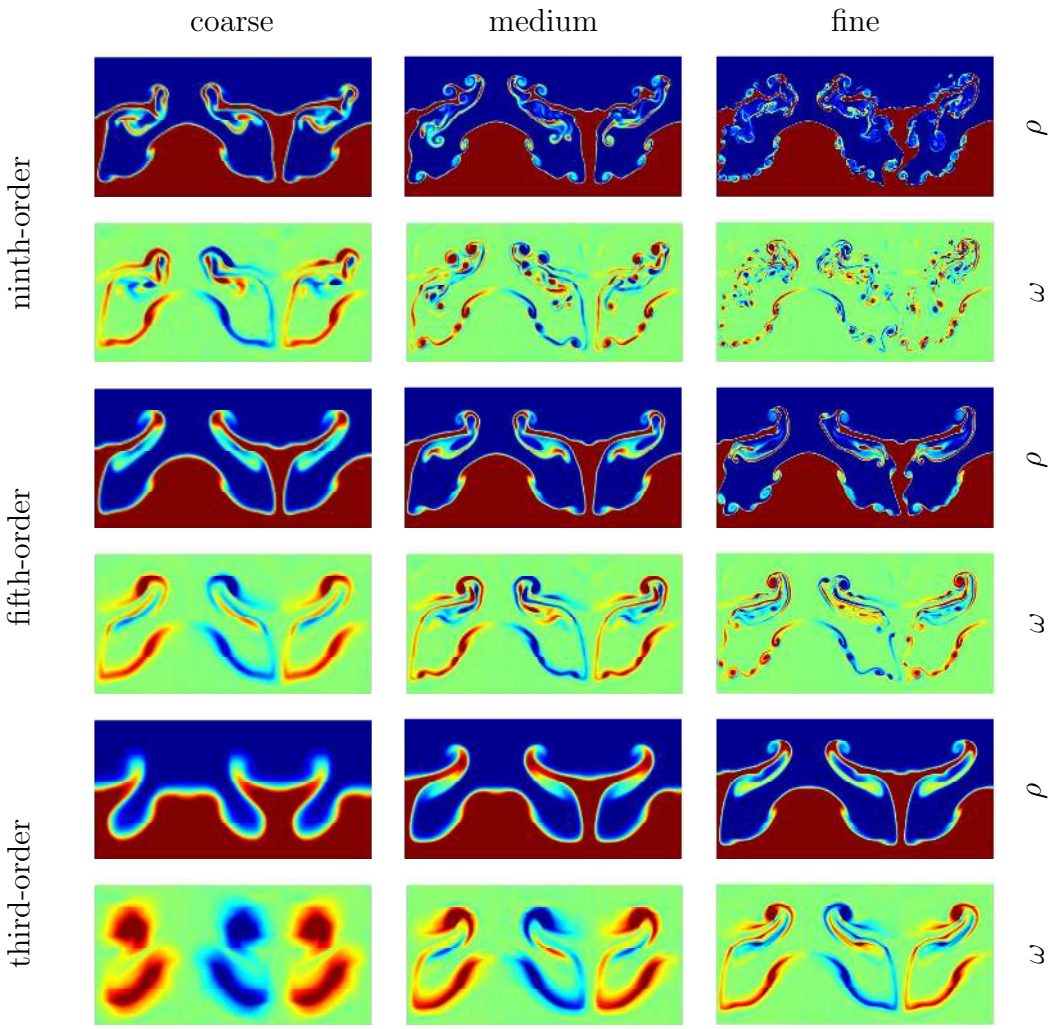

Fig. 3. The density and vorticity fields at 7 ms (after reshock) from the third-, fifth- and ninth-order simulations on the coarse, medium and fine grids.

ments [3,33–35]. A qualitative correspondence in both ρ and ω can be seen between simulations along a diagonal, so that doubling the resolution approximately corresponds to doubling the order (as also found in Rayleigh-Taylor instability and double Mach reflection simulations [11]).

Figure 3 continues the comparison of ρ and ω following reshock (which occurs at $\approx$ 6.4 ms) at 7 ms, with the bubble transforming into a spike and vice versa through inversion due to the deposition of vorticity of opposite sign during reshock. The SF_6 spike penetrates into the air(acetone) and becomes narrower as it transforms into a bubble. As the order and resolution increase, additional finer-scale complex structures appear. This is also reflected in ω, which shows that strong positive and negative cores transition into vortex bilayers, and then into fragmented cores.

Following reshock, a transmitted shock enters the air(acetone) and a reflected

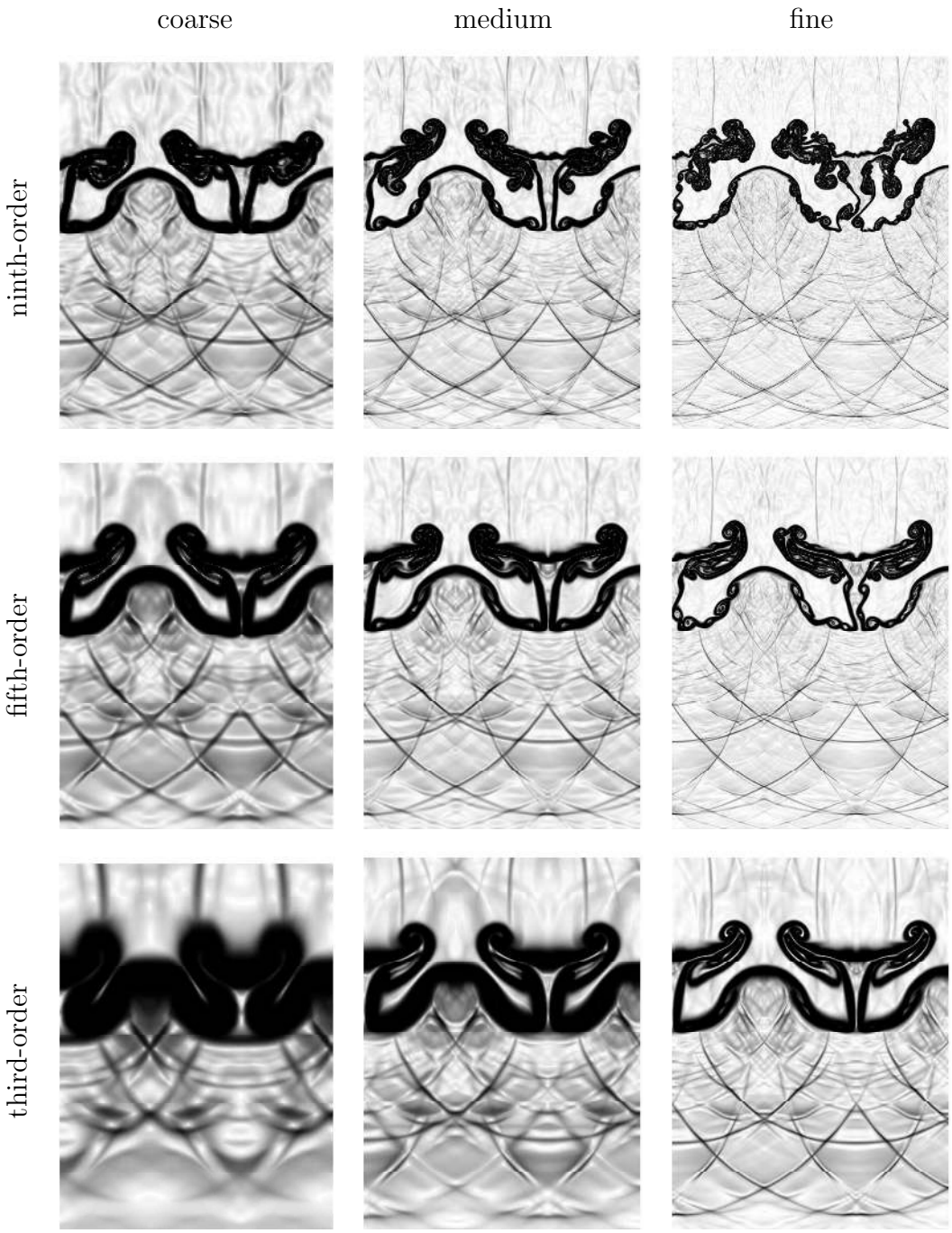

Fig. 4. The simulated density Schlieren fields at 7 ms (after reshock) from the third-, fifth- and ninth-order simulations on the coarse, medium and fine grids.

rarefaction enters the SF_6, resulting in a complex system of reflected and transmitted waves that further contribute to the development of the instability and to mixing. To visualize these waves, as well as the complex structures on

the interface, the simulated density Schlieren fields [21]

$$\Phi(x,y,t) = \exp\left[-\alpha(m)\,\frac{|\boldsymbol{\nabla}\rho|}{\max|\boldsymbol{\nabla}\rho|}\right] \quad , \quad \alpha(m) = \begin{cases} 20 & \text{if } m > m^* \\ 100 & \text{if } m < m^* \end{cases}, \qquad (7)$$

where m is the mass fraction of SF_6 and $m^* = 0.25$ is the threshold, are shown in Fig. 4 at 7 ms. A complex system of curved intersecting waves exists in the SF_6 gas, corresponding to the reflected rarefaction, together with fine-scale structure surrounding the spike. As the order and resolution increase, the waves become sharper and additional structures appear on the interface. Shock focusing on the reshocked spike can also be seen.

The density at 12 ms in Fig. 5 shows the evolution of the main spike, which develops several roll-ups and additional complex structure. The difference among the orders and resolutions is now significant. In particular, the WENO3 and WENO5C simulations retain significant coherency and symmetry, with a clearly identifiable dominant structure. Beginning with the WENO5M simulation, a progressive loss of symmetry occurs, together with the development of increasingly finer-scale structure. This is also reflected in ω, in which large-scale organized strong cores are replaced by progressively fragmented and more concentrated cores. The vorticity dynamics is in qualitative agreement with two-dimensional turbulence phenomenology [4]. As the order and resolution are increased, more fragmented, smaller-scale structures form. By contrast, as the resolution is decreased, large persistent vortical structures form. The WENO3 results are characteristic of simulations with large numerical diffusion, as well as of simulations that are spatially underresolved. Instead, the fifth- and ninth-order simulations exhibit symmetry breaking (also reported in other simulations with reshock using lower order methods [10,36] and in Rayleigh-Taylor instability simulations using the ninth-order WENO method [11]), which can be attributed to numerical instabilities not damped by the intrinsic dissipation in the WENO method.

Figure 6 illustrates the reshock process, showing the development of complex structures during the spike roll-up at 6, 6.6, 6.8 and 7 ms from the fine grid simulations. Prior to reshock at 6 ms, the WENO9 simulations exhibit complex structures within the roll-up: such structures are also visible in the inner core of the WENO5 simulations and are absent in the WENO3 simulations. During reshock, the roll-up is compressed at 6.6 ms and forms complex structures later. The WENO3 and WENO5 simulations retain a single dominant structure, while the WENO9 simulations exhibit fragmentation.

The dynamics during reshock can be further elucidated by considering the vorticity field $\omega(x,y)$ and the baroclinic vorticity production $\mathcal{P}(x,y)$ during reshock, which are shown in Fig. 7 at the same times as the density fields in Fig. 6. At 6 ms, the WENO5F and WENO9F vorticities exhibit complex roll

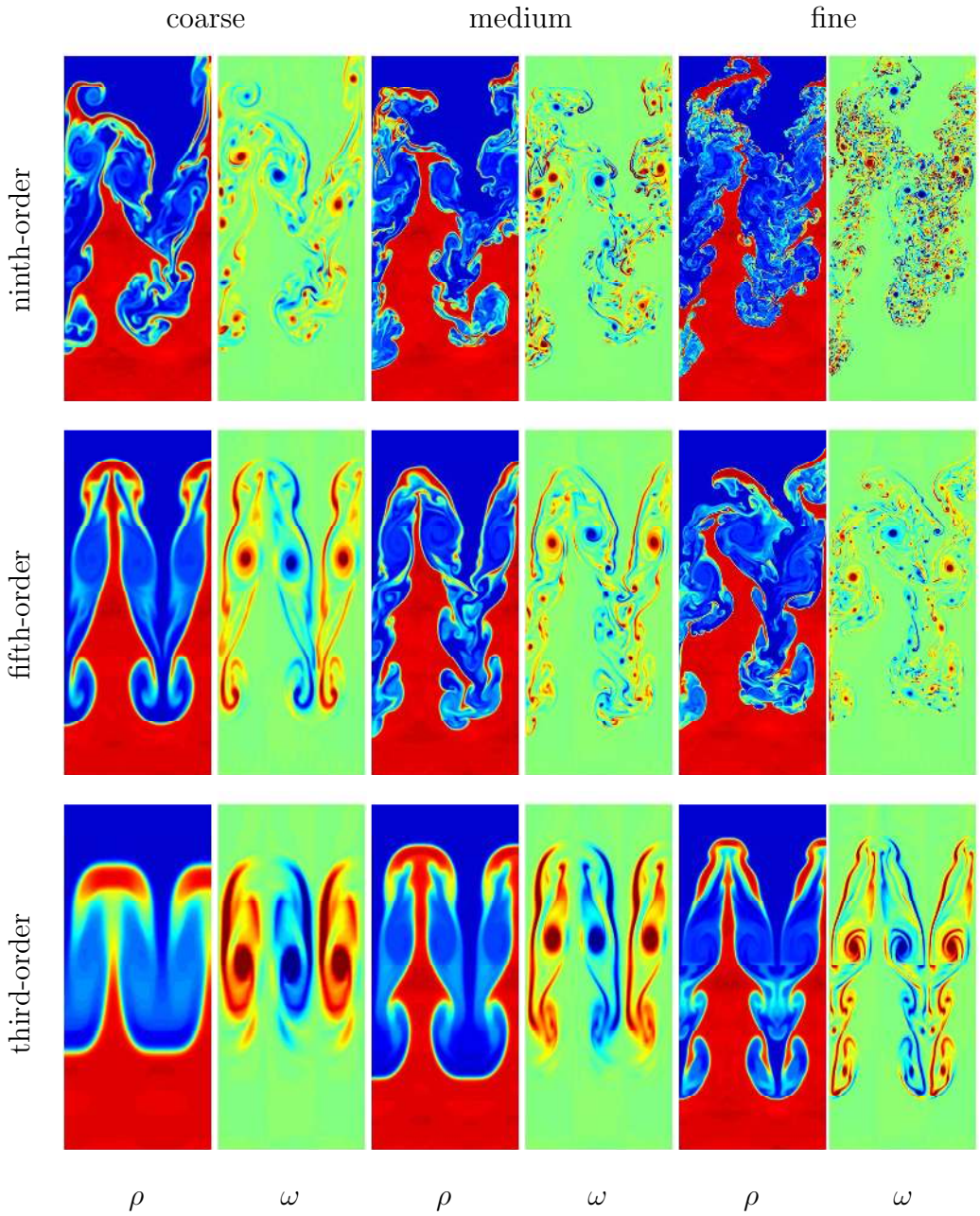

Fig. 5. The density and vorticity fields at 12 ms (late time following reshock) from the third-, fifth- and ninth-order simulations on the coarse, medium and fine grids.

ups with regions of negative vorticity surrounded by positive vorticity forming a vortex bilayer. This generation of positive vorticity is due to baroclinic vorticity production. The WENO3 simulations only show a strong negative core, and the baroclinic production does not exhibit the complex features in the WENO5 and WENO9 simulations. Just after reshock at 6.6 ms, the strong negative core is significantly weakened and a layer of positive vorticity is deposited on the tip of the spike: this layer is particularly evident in the WENO3 and WENO5 simulations, and is thinner in the WENO9 simulations. The vor-

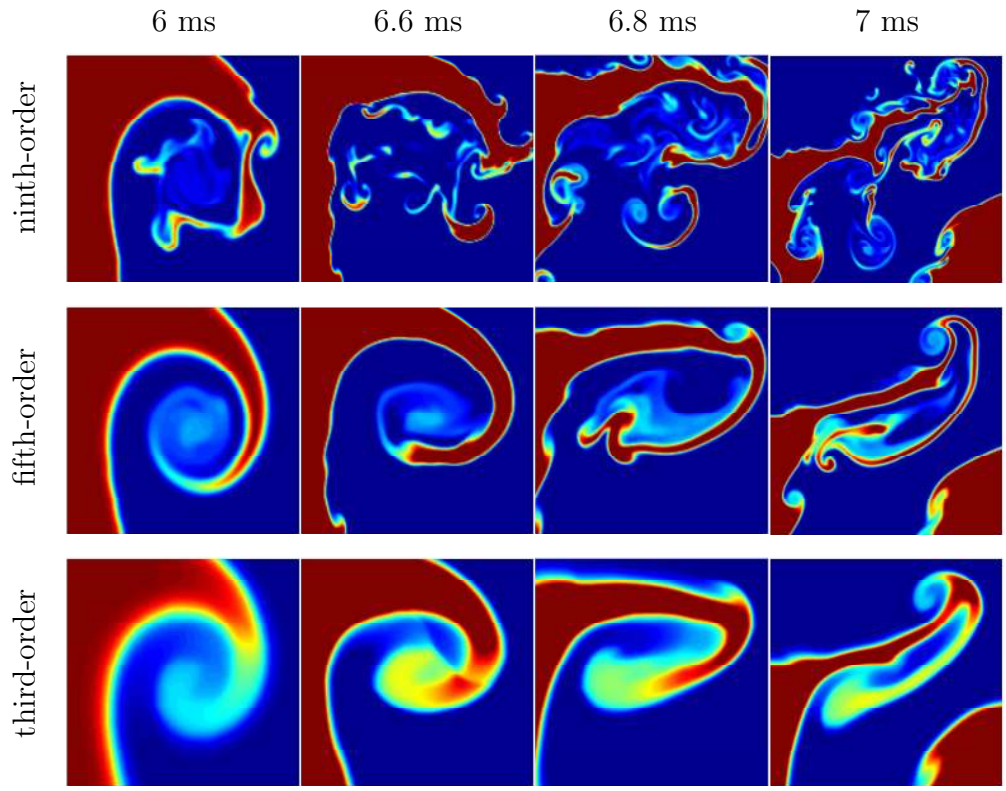

Fig. 6. Details of the roll-up in the density field from the ninth-, fifth- and third-order fine grid simulations at 6, 6.6, 6.8 and 7 ms.

ticity forms cores at 6.8 and 7 ms, with the WENO9 cores more spatially compact than those in the other simulations. The baroclinic vorticity production is also fragmented in the WENO9 simulations. These fields illustrate the significant difference in the vorticity dynamics for simulations including reshock performed using different orders and resolutions.

4 The effects of order and resolution on the mixing layer width and circulation deposition

The effects of order and resolution on the mixing layer width and the circulation deposition are considered in this section. It is shown that the dependence on order and resolution is most pronounced following reshock, with the differences among the simulations increasing with time.

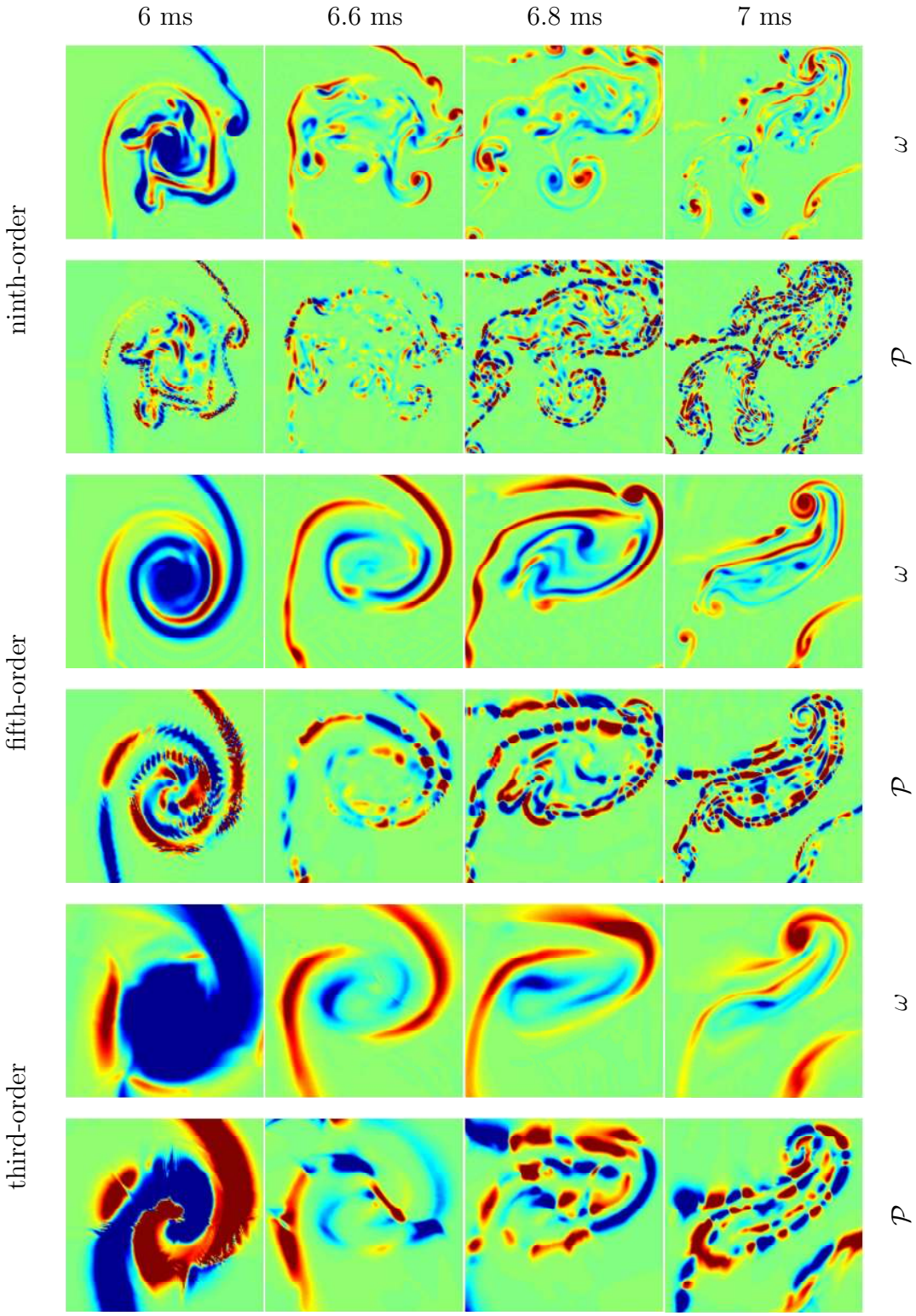

Fig. 7. Details of the roll-up in the vorticity and in the baroclinic vorticity production fields from the ninth-, fifth- and third-order fine grid simulations at 6, 6.6, 6.8 and 7 ms.

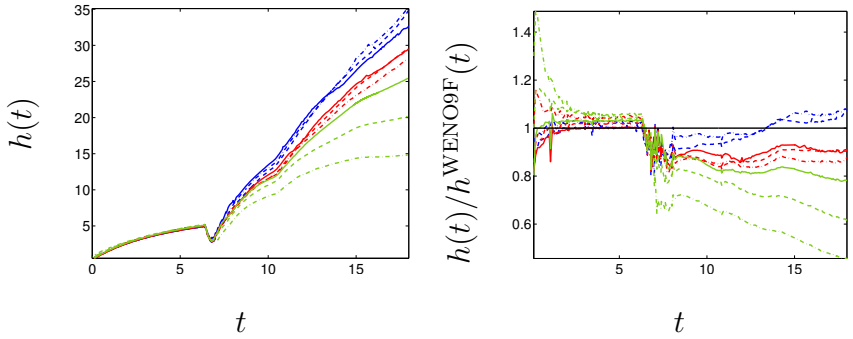

Fig. 8. Comparison of the time-evolution of the mixing layer width when the order and resolution are varied (left). The mixing layer widths normalized by that from the WENO9F simulation are also shown (right). Quantities obtained using the WENO3, WENO5 and WENO9 simulations are shown in green, red and blue, respectively; quantities obtained on the fine, medium and coarse grid are shown using a solid, dashed and dash-dot line, respectively.

4.1 The mixing layer width

To determine the mixing layer width, consider the mole fraction $X(x,y,t) = m(x,y,t)M_1/\{[1-m(x,y,t)]\,M_2 + m(x,y,t)M_1\}$, where m is the mass fraction of SF_6 and M_1 and M_2 are the constant molecular weights of air(acetone) and SF_6, respectively. Spatially-averaging X in the y-direction gives

$$\overline{X}(x,t) = \frac{1}{L_y}\int_0^{L_y} X(x,y,t)\,\mathrm{d}y\,, \tag{8}$$

where L_y is the spanwise width of the domain. The spike and bubble locations, $\ell_s(t)$ and $\ell_b(t)$, are defined as the x position where $\overline{X} \geq \epsilon$ and $\overline{X} \leq 1-\epsilon$, respectively, with $\epsilon = 0.01$ in the present investigation. The total mixing layer width is the difference between the bubble and spike positions, $h(t) = \ell_b(t) - \ell_s(t)$.

The dependence of the mixing layer width $h(t)$ on the order and resolution is shown in Fig. 8 up to 18 ms (left). Also shown are the widths normalized by the WENO9F width (right). Prior to reshock, $h(t)$ weakly depends on the order and resolution: the flow is dominated by a single, large-scale bubble or spike, the front of which is not significantly affected by dissipation. The dependence on order and resolution becomes significant following reshock, with $h(t)$ decreasing for lower orders and resolutions. Prior to the arrival of the reflected rarefaction at ≈ 11 ms, the widths become closer as the order and resolution increase. The differences are further amplified by the arrival of the reflected rarefaction and increase later in time. At late times, the WENO3 widths differ by as much as ≈ 5 cm as the grid is refined. By contrast, the WENO5 and WENO9 widths differ by ≈ 1 cm. The normalized widths exhibit evidence for 'convergence' as the ratios approach unity for the WENO9 simulations.

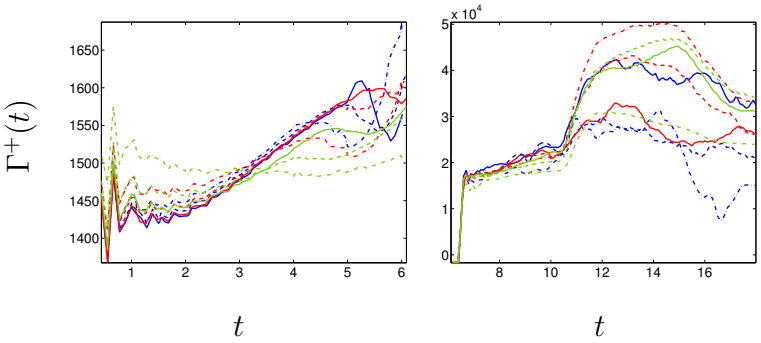

Fig. 9. Comparison of the time-evolution of the positive circulation Γ^+ before reshock (left) and after reshock (right) when the order and resolution are varied. See Fig. 8 for the legend.

4.2 The interfacial circulation deposition

The vorticity deposited by the shock on the interface and by baroclinic vorticity production, can be quantified using the positive and negative circulation. As the vorticity field and the outward area element are parallel, the positive and negative circulations $\Gamma^{\pm}$ can be approximated on the rectangular grid with spacing Δx and Δy over $U^+ = \{\lambda/2 < y_j \leq \lambda\}$ and $U^- = \{0 < y_j \leq \lambda/2\}$ [4]:

$$\Gamma^{\pm}(t) = \sum_{i=1}^{N_x} \sum_{j=1}^{N_y} \omega(x_i, y_j, t)|_{y_j \in U^{\pm}} \, \Delta x \, \Delta y \, . \tag{9}$$

Before reshock, the positive circulations Γ^+ in Fig. 9 are similar, increasing steadily due to baroclinic vorticity production. As the spike rolls up and vorticity of opposite sign is created within the roll ups, Γ^+ stops increasing and a slight decrease is observed in the WENO9F simulation. Instead, the WENO3C circulation is nearly constant across the layer, as the baroclinic vorticity production is small. A sharp increase in Γ^+ occurs at reshock, corresponding to the rapid deposition of additional vorticity on the interface. Following reshock and prior to the arrival of the reflected rarefaction at ≈ 11 ms, Γ^+ from all of the simulations are qualitatively similar, exhibiting a steady increase due to the additional vorticity deposition. After the arrival of the reflected rarefaction, symmetry breaks and the regions $U^{\pm}$ no longer contain vorticity of a single sign, resulting in large differences in Γ^+ for $t > 11$ ms.

5 The effects of order and resolution on mixing profiles, production and mixing fractions, energy spectra, statistics and probability distribution functions

The effects of order and resolution on mixing profiles, production and mixing fractions, energy spectra, statistics and probability distribution functions are quantified in this section. The comparisons of these quantities are conducted at 6 ms immediately before reshock, at 7 ms immediately after reshock, and at 18 ms at late times following reshock. To facilitate the comparison of the mixing profiles, and the production and mixing fractions, the streamwise coordinate is recentered by the midpoint $x_{\rm mid}(t)$ between the bubble and spike position, and normalized by the mixing layer width $h(t)$. Most of the effects on the quantities considered can be interpreted in terms of the relative numerical dissipation, with increasing order and increasing resolution associated with decreasing dissipation. The results demonstrate that different characterizations of mixing are possible depending on the order and resolution: *caution must be exercised when interpreting the results of Richtmyer-Meshkov instability simulations as described by the Euler equations.*

5.1 The mixing profiles

Up to 7 ms, the mole fraction profiles $\overline{X}(x,t)$ in Fig. 10 agree at sufficiently high resolution. A more disordered structure is observed at late times: as $\overline{X}$ measures the distribution of mass across the mixing layer, the differences at 18 ms are due to different mass distributions among the different simulations. On average, $\overline{X}$ approaches a nearly linear profile at late times.

Figure 10 also shows the molecular mixing profile [37,38]

$$\theta(x,t) = \frac{\overline{f_1 f_2}}{\overline{f_1}\,\overline{f_2}} \quad \text{where} \quad f_1(x,y,t) \equiv \frac{\frac{m(x,y,t)}{\rho_1}}{\frac{m(x,y,t)}{\rho_1} + \frac{1-m(x,y,t)}{\rho_2}} \tag{10}$$

and $f_2 = 1 - f_1$ are the volume fractions of fluid 1 [air(acetone)] and fluid 2 (SF_6), and $\overline{\phi}$ signifies the spatial average of $\phi(x,y,t)$ over the y-direction [see Eq. (8)]. The molecular mixing profile $\theta(x,t)$ is highly sensitivity to the order and resolution. The large peak on the air(acetone) side at 6 ms corresponds to the spike roll-up: all of the simulations approximately capture this effect. In the regions near the stem of the spike, the WENO9 simulations yield larger θ and a sharper transition near the boundaries than the WENO3 and WENO5 simulations, consistent with higher-order simulations having sharper interfaces and less numerical diffusion. Compression caused by reshock increases θ at 7 ms. The profile is shifted toward the air(acetone), corresponding to enhanced

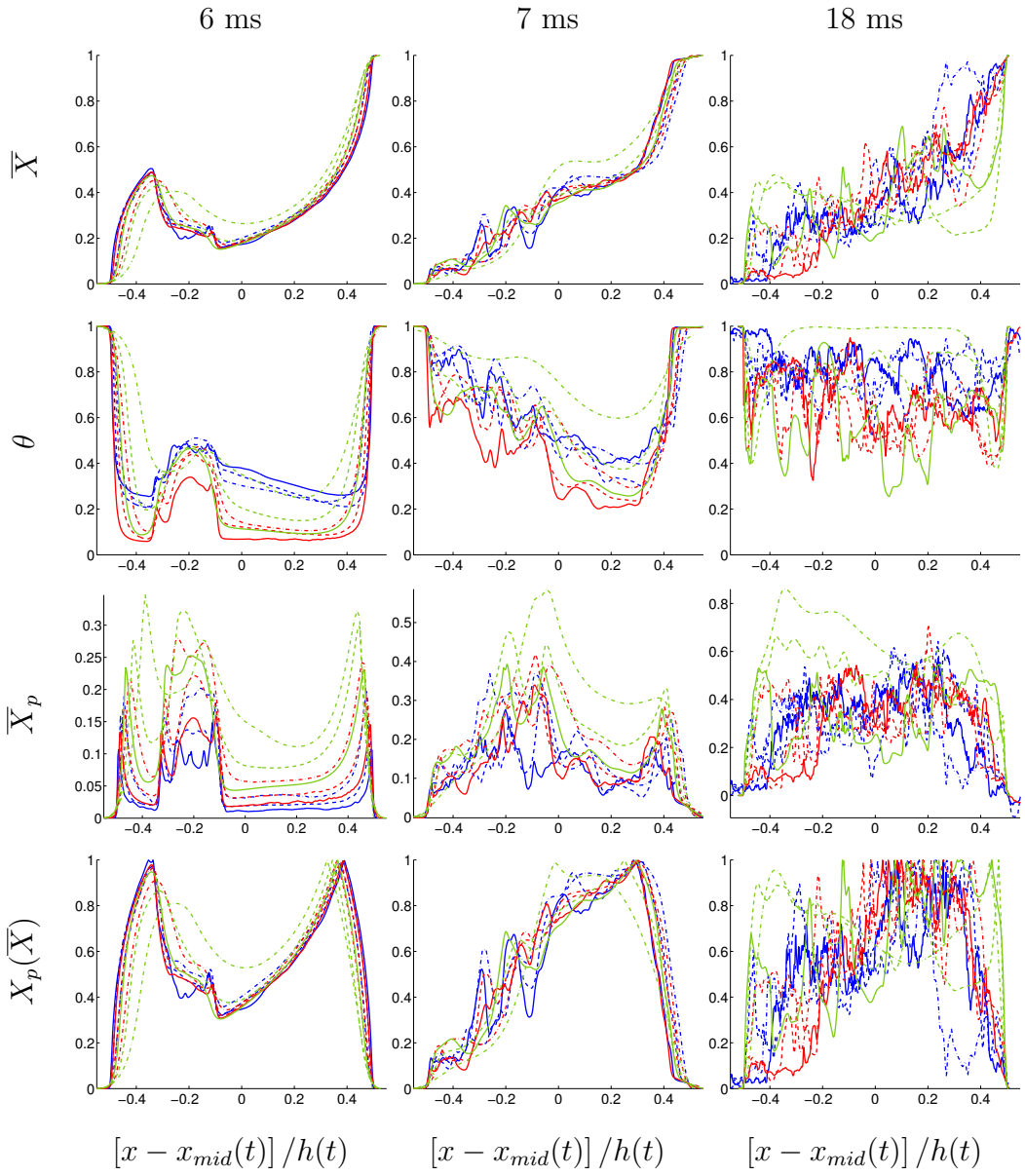

Fig. 10. Comparison of the averaged mole fraction profile $\overline{X}$, molecular mixing profile θ, averaged product mole fraction profile $\overline{X}_p$ and maximum product mole fraction profile $X_p(\overline{X})$ across the layer at 6, 7 and 18 ms when the order and resolution are varied. See Fig. 8 for the legend.

mixing near the spike, while less mixing occurs as the new spike of SF_6 emerges due to the inversion process. The effects of the different mass distribution and mixing across the layer among the simulations are evident at 18 ms, with $\theta \sim 0.75$–0.8 on average for the WENO9 simulations.

A quantitative measure of mixing can be defined as follows. Suppose that the two fluids undergo a fast kinetic reaction, so that the amount of product

produced is [39,40]

$$X_p(x,y,t) = \begin{cases} \frac{X(x,y,t)}{X_s} & \text{if } X \leq X_s \\ \frac{1-X(x,y,t)}{1-X_s} & \text{if } X > X_s \end{cases} \tag{11}$$

with $X_s = 1/2$, indicating that the product is composed of one mole of each 'reactant' (heavy or light fluid), and is limited by the amount of reactant. The averaged product mole fraction profile $\overline{X}_p(x,t)$, which measures how well mixed the two 'reactants' are, is shown in Fig. 10. Values near unity indicate that complete mixing has occurred, resulting in the formation of product, while values near zero correspond to little mixing and product formation (here, numerically-induced mixing is a surrogate for chemical reactions). At 6 ms, $\overline{X}_p$ is strongly peaked, corresponding to the spike roll-up. The magnitude of the peak shows that the WENO9, WENO5 and WENO3 simulations correspond to progressively increased mixing in the roll-up. Similar behavior is also observed along the stem of the spike and at the tip of the bubble and spike. These results are consistent with reduced numerical diffusion and diffusion-induced mixing in the WENO9 simulations. At 7 ms, $\overline{X}_p$ is peaked near the air(acetone) (corresponding to the compressed spike roll-up) with a smaller value near the SF_6 (corresponding to the emergence of the spike due to inversion). At 18 ms, the variations in $\overline{X}_p$ across the layer are associated with the different underlying small-scale structures at late times.

Also shown in Fig. 10 is the maximum product mole fraction profile $X_p(\overline{X})$, which corresponds to the total amount of product obtained if both fluids were homogeneously mixed. At 6 ms, $X_p(\overline{X})$ exhibits large peaks near the bubble and spike tips, corresponding to the small diffusive mixing in these locations. A small peak corresponding to the center of the roll-up is captured by all of the simulations, with the exception of the WENO9F simulation, which results from the additional structure within the roll-ups. At 7 ms, all of the profiles are very similar and have a large peak close to the SF_6 side, corresponding to the emergence of the spike. The oscillatory profiles at 18 ms result from the underlying small-scale structure within the mixing layer.

5.2 The production and mixing fractions

Using Eq. (11), the total chemical product $P_t(t)$, maximum chemical product $P_m(t)$, and mixing fractions $\Xi(t)$ and $\Theta(t)$ are defined as

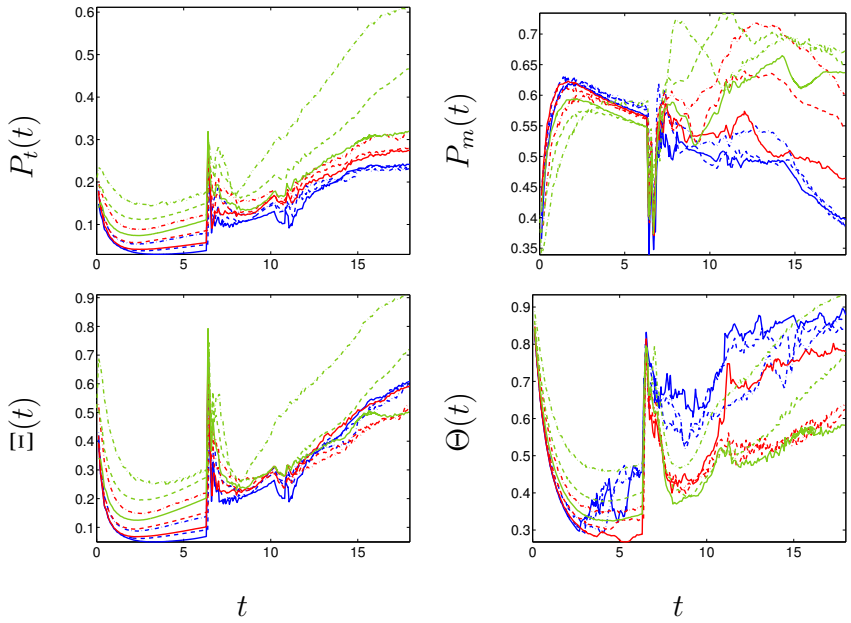

Fig. 11. Comparison of the time-evolution of the production and mixing fractions, $P_t(t)$, $P_m(t)$, $\Xi(t)$ and $\Theta(t)$, when the order and resolution are varied. See Fig. 8 for the legend.

$$P_t(t) = \frac{1}{h(t)} \int_{\ell_s(t)}^{\ell_b(t)} \overline{X}_p \, \mathrm{d}x \quad , \quad P_m(t) = \frac{1}{h(t)} \int_{\ell_s(t)}^{\ell_b(t)} X_p(\overline{X}) \, \mathrm{d}x \, , \tag{12}$$

$$\Xi(t) = \frac{P_t(t)}{P_m(t)} \quad , \quad \Theta(t) = \frac{\int_{\ell_s(t)}^{\ell_b(t)} \overline{f_1 \; f_2} \, \mathrm{d}x}{\int_{\ell_s(t)}^{\ell_b(t)} \overline{f_1} \, \overline{f_2} \, \mathrm{d}x} \, ; \tag{13}$$

$P_m(t) > P_t(t)$ is the amount of product obtained if both 'reactants' were homogeneously mixed. Values near unity correspond to complete mixing for both Ξ and Θ, while values near zero correspond to little mixing.

The total chemical product $P_t(t)$ in Fig. 11 exhibits a rapid decrease following the initial passage of the shock, followed by a steady increase. Reshock causes a sharp increase followed by a rapid decrease. A steady increase subsequently occurs, with a small decrease corresponding to the arrival of the reflected rarefaction at ≈ 11 ms, which stretches the interface but does not contribute to mixing. Consequently, $\overline{X}_p$ decreases due to the arrival of the reflected rarefaction, resulting in smaller P_t. All of the simulations exhibit similar qualitative behavior, with the WENO3, WENO5 and WENO9 simulations giving progressively smaller values resulting from the correspondingly smaller $\overline{X}_p$.

The maximum chemical product, $P_m(t)$, in Fig. 11 exhibits different behavior than $P_t(t)$. The passage of the incident shock causes a rapid increase followed by a steady decrease caused by the formation of the spike, which effectively "demixes" the interface. Reshock causes a rapid decrease, followed by a rapid increase. Following reshock, the values are quite different. The WENO3 simu-

lations show a rapid increase followed by a steady decrease. The WENO5C and WENO5M simulations show an increase until ≈ 11 ms, followed by a decrease; the WENO5F and WENO9 simulations show a steady decrease. This behavior is a consequence of the different structures in the mixing layer following the passage of the shock. In particular, the WENO9 simulations show features in largely unmixed regions, while the WENO3 simulations show significant mixing at all times.

The mixing fractions $\Xi(t)$ and $\Theta(t)$ are also shown in Fig. 11. Although both quantities provide similar information concerning the mixedness of the fluids, $\Xi(t)$ and $\Theta(t)$ obtained using different orders and resolutions exhibit significant differences. First, Ξ rapidly decreases following passage of the incident shock, and then steadily increases. Reshock causes a rapid increase followed by a rapid decrease, and then a steady increase indicating increased mixing near the interface. The values of Ξ can be interpreted in terms of the behavior of the total and maximum chemical product, P_t and P_m. By contrast, following the passage of the shock, Θ rapidly decays and then increases. The WENO9F simulation exhibits quite different behavior, as Θ is influenced by the structures within the roll-ups. Reshock rapidly increases Θ, followed by a rapid decrease in the WENO3 and WENO5 simulations. The decrease is not as large in the WENO9 simulations. A steady increase in Θ then follows. These results are again a consequence of the different small-scale structures in the flow following reshock. In particular, the large unmixed regions in the WENO9 simulations result in larger Θ.

5.3 The energy spectra

The effects of order and resolution on the distribution of energy among different scales can be quantified by energy spectra associated with fluctuations. Let $\overline{\phi}(x,t)$ denote an instantaneous average of a field $\phi(x,y,t)$ over the symmetric (spanwise) direction y with length L_y. Define the corresponding fluctuating field $\phi(x,y,t)' \equiv \phi(x,y,t) - \overline{\phi}(x,t)$. Introduce the instantaneous density-weighted average $\widetilde{\phi}(x,t) \equiv \overline{\rho\phi}/\overline{\rho}$ and the corresponding fluctuating field $\phi(x,y,t)'' \equiv \phi(x,y,t) - \widetilde{\phi}(x,t)$. The energy associated with each Fourier mode k is obtained by averaging over the extent of the mixing layer to obtain the one-dimensional energy spectrum of ϕ,

$$E_{\phi\phi}(k,t) = \frac{1}{2\,h(t)} \int_{\ell_s(t)}^{\ell_b(t)} \left|\widehat{\phi}(k,x,t)\right|^2 \,\mathrm{d}x\,, \tag{14}$$

where $\widehat{\phi}(k,x,t) = \frac{1}{2\pi}\int_{-\infty}^{\infty} \phi(x,y,t)\exp(-iky)\,\mathrm{d}y$ is the Fourier coefficient of the 2π-periodic function $\phi(x,y,t)$ in the y direction. Numerically, the discrete (sine) cosine transform is used to compute the Fourier coefficients using the (anti-) symmetry property of the underlying data in the spanwise direction.

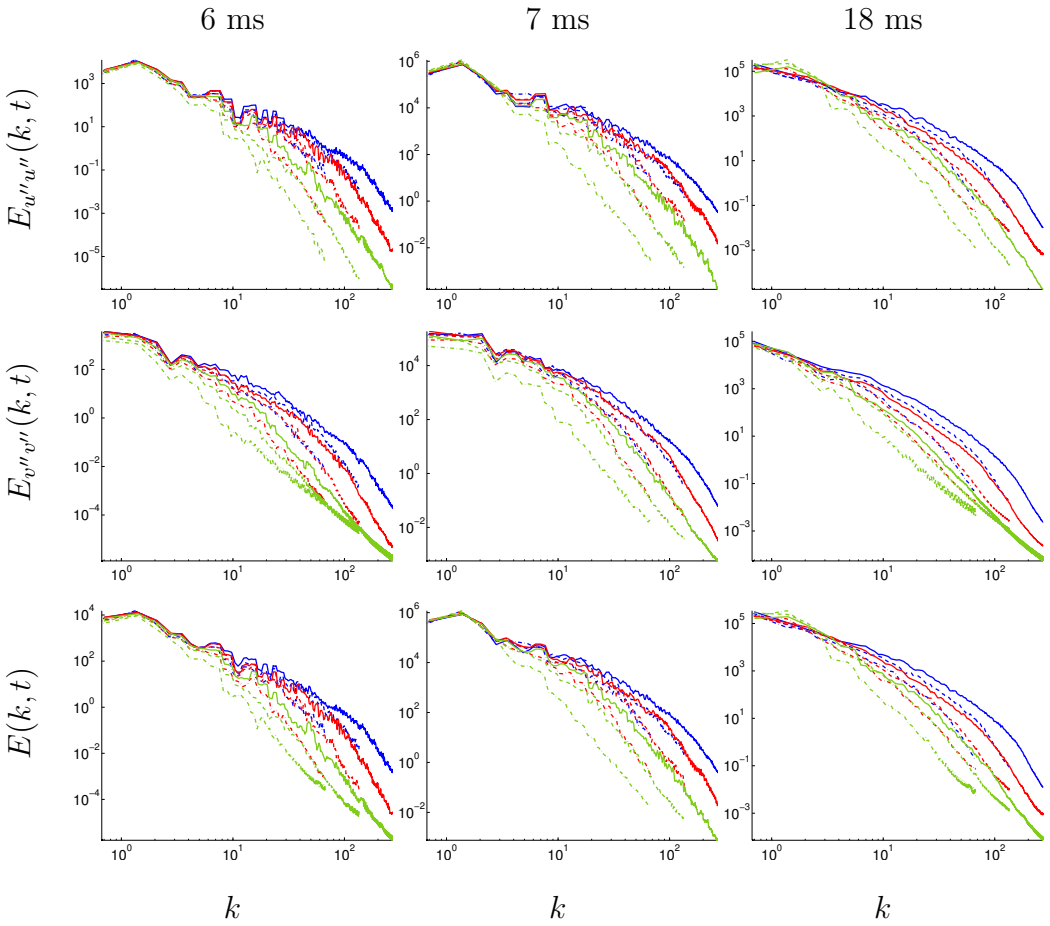

Fig. 12. Comparison of the streamwise and spanwise turbulent kinetic energy spectra $E_{u''u''}(k,t)$ and $E_{v''v''}(k,t)$ and turbulent kinetic energy spectrum $E(k,t)$ at 6, 7 and 18 ms when the order and resolution are varied. See Fig. 8 for the legend.

The streamwise and spanwise turbulent kinetic energy spectra, $E_{u''u''}(k,t)$ and $E_{v''v''}(k,t)$, in Fig. 12 both depend on the order and resolution. The large-scale (small k) spectra are very similar across the simulations. The variations in the spectra decrease at later times, and at 18 ms the spectra are smooth. Higher-order higher-resolution spectra have increased energy content at intermediate k. The WENO5F and WENO9M spectra are nearly the same, consistent with the fact that approximately doubling the order or doubling the resolution yields very similar flow features. The turbulent kinetic energy spectrum, $E(k,t) = E_{u''u''}(k,t) + E_{v''v''}(k,t)$, is also shown, the behavior of which is dominated by the streamwise component at 6 and 7 ms.

The turbulent enstrophy spectrum $E_{\omega''\omega''}(k,t)$ in Fig. 13 is much more sensitive than $E(k,t)$: as the order and the resolution increase, the turbulent enstrophy content of all scales increases. The WENO9F turbulent enstrophy spectrum differs from the WENO3C spectrum by an order of magnitude in the large scales and by several orders of magnitude in the intermediate and small

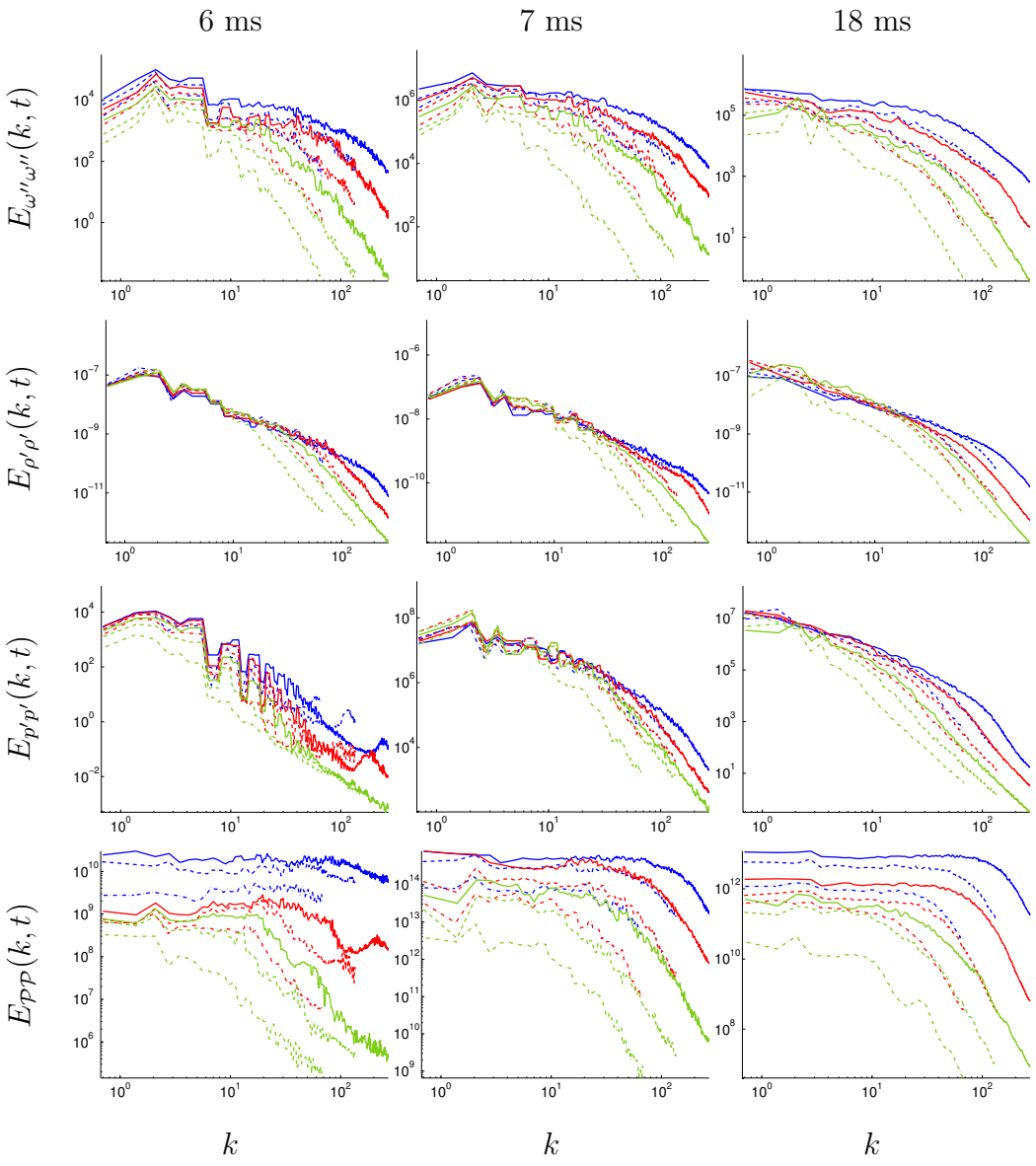

Fig. 13. Comparison of the turbulent enstrophy spectrum $E_{\omega''\omega''}(k,t)$, density variance spectrum $E_{\rho'\rho'}(k,t)$, pressure variance spectrum $E_{p'p'}(k,t)$, and baroclinic vorticity production variance spectrum $E_{\mathcal{PP}}(k,t)$ at 6, 7 and 18 ms when the order and resolution are varied. See Fig. 8 for the legend.

scales. As shown in Fig. 5, the vorticity corresponding to higher orders and higher resolutions increases in magnitude and is more localized, resulting in the increased spectra. At 18 ms, the oscillatory modes have been damped out and the spectra begin to decay. The lower-order lower-resolution spectra are much steeper than the higher-order higher-resolution spectra. As the vorticity is constructed from the difference of the velocity gradients, $\partial u/\partial y$ and $\partial v/\partial x$, its large k modes are more sensitive to numerical damping than are primitive fields such as the velocity: this sensitivity is amplified quadratically, as the enstrophy is proportional to ω^2.

The density variance spectra in Fig. 13 are similar at small k. A steep decrease occurs at progressively larger k as the order and resolution increase. This is particularly evident at 18 ms when all oscillatory modes have been damped out. By contrast, the pressure variance spectrum $E_{p'p'}(k,t)$ in Fig. 13 exhibits differences even in the small k range, with higher order and resolution resulting in increased values. The steep decline in the intermediate- to large-k spectra can be related to the numerical dissipation, which smooths out fluctuations at large k. The lower-order lower-resolution spectra are steeper than the higher-order higher-resolution spectra.

The baroclinic vorticity production variance spectra $E_{\mathcal{P}\mathcal{P}}(k,t)$ in Fig. 13 have nearly constant values over a large range of k. The spectra decrease rapidly at large k. Higher-order higher-resolution spectra remain nearly constant over a larger extent of scales, and are larger in magnitude. By contrast, lower-order lower-resolution spectra decay very rapidly with increasing k, and have smaller values. These results are consistent with the vorticity and baroclinic vorticity production evolution shown in Fig. 7, where $\mathcal{P}(x,y,t)$ from higher-order high-resolution simulations exhibits fragmentation into regions of large positive and negative values. This, in turn, generates vorticity of opposite sign on the interface which contributes to mixing and to a mixing layer with complex structure: increased baroclinic vorticity production in higher-order higher-resolution simulations is correlated with increased mixing and proliferation of complex structures within the layer. As the baroclinic vorticity production variance is proportional to $(\boldsymbol{\nabla}\rho \times \boldsymbol{\nabla}p)^2$, the large wavenumber modes of its spectrum are highly sensitive to numerical damping.

5.4 The statistics

The effects of order and resolution on the statistics

$$E_{\phi\phi}(t) = \int_0^{k_{\max}} E_{\phi\phi}(k,t)\,\mathrm{d}k\,, \tag{15}$$

including the streamwise and spanwise turbulent kinetic energy and the total turbulent kinetic energy are shown in Fig. 14 as a function of time. The turbulent enstrophy, the density and pressure variance, and the baroclinic vorticity production variance are shown in Fig. 15 as a function of time.

The streamwise turbulent kinetic energy $E_{u''u''}(t) = \widetilde{u''^2}/2$ decreases prior to reshock, corresponding to the evolution of the roll-up on the spike. As the order and resolution increase, larger energies are obtained. Reshock causes a rapid decrease, followed by a much slower decrease, with all of the simulations giving similar values. Following the arrival of the reflected rarefaction at $\approx$ 11 ms, the lower-order simulations have larger energies. By contrast, the

spanwise turbulent kinetic energy $E_{v''v''}(t) = \widetilde{v''^2}/2$ increases prior to reshock, corresponding to the development of the roll-up. The increase is more pronounced in the higher-order higher-resolution simulations as the roll-up develops complex structures. The energy increases rapidly at reshock and then decays, with a faster decay for the lower-order lower-resolution simulations. The turbulent kinetic energy $E(t) = \left(\widetilde{u''^2} + \widetilde{v''^2}\right)/2$ behaves similarly to its dominant streamwise component $E_{u''u''}(t)$.

The turbulent enstrophy $E_{\omega''\omega''}(t) = \widetilde{\omega''^2}/2$ in Fig. 15 exhibits significant sensitivity to the order and resolution. The turbulent enstrophy decreases prior to reshock, with a faster decrease for the lower-order lower-resolution simulations. The higher-order higher-resolution simulations exhibit a smaller decrease, as additional vorticity is deposited in the roll-up by baroclinic production, which creates the vortex bilayers in Fig. 7. Reshock causes a rapid increase, followed by a steady decrease. Large differences are also observed following reshock, as the rapid increase in $E_{\omega''\omega''}(t)$ caused by reshock is smaller in the lower-order lower-resolution simulations. As vorticity fluctuations are responsible for the kinetic energy dissipation and the transfer of energy to smaller scales, a larger enstrophy from higher-order higher-resolution simulations is associated with the presence of additional small-scale structures.

The density variance $E_{\rho'\rho'}(t) = \overline{\rho'^2}/2$ in Fig. 15 is sensitive to the order and resolution, particularly at late times. Prior to reshock, lower-order lower-resolution simulations have smaller values, consistent with the suppression of small scales by increased numerical dissipation. A rapid increase after reshock is followed by a slow decrease, which becomes more pronounced following the arrival of the reflected rarefaction at ≈ 11 ms, amplifying the difference in $E_{\rho'\rho'}(t)$ across orders. The WENO3C and WENO3M density variance is rapidly damped, resulting in a rapid decrease. The pressure variance $E_{p'p'}(t)$ exhibits little sensitivity to the order and resolution, prior to and following reshock, and at late times.

The baroclinic vorticity production variance $E_{\mathcal{PP}}(t)$ in Fig. 15 is highly sensitive to the order and resolution, increasing prior to reshock in the WENO9M and WENO9F simulations and decreasing in all of the other simulations. The increase in the WENO9 simulations is due to the secondary baroclinic vorticity deposition in the roll-up, resulting in the formation of complex structures shown in Fig. 6. These structures are not captured in the other simulations. Reshock strongly increases $E_{\mathcal{PP}}(t)$, which is followed by a decay. The arrival of the reflected rarefaction at ≈ 11 ms further increases $E_{\mathcal{PP}}(t)$. Following reshock, the $E_{\mathcal{PP}}(t)$ from the WENO5F and WENO9M simulations are very similar. Prior to reshock, a distinct difference is found between the WENO5 and WENO9 simulations.

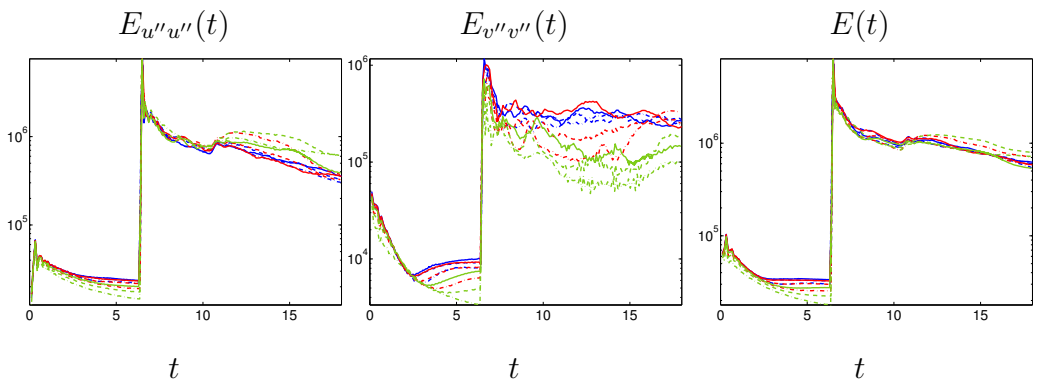

Fig. 14. Comparison of the time-evolution of the streamwise turbulent kinetic energy, spanwise turbulent kinetic energy and total kinetic energy, $E_{u''u''}(t)$, $E_{v''v''}(t)$ and $E(t)$, when the order and resolution are varied. See Fig. 8 for the legend.

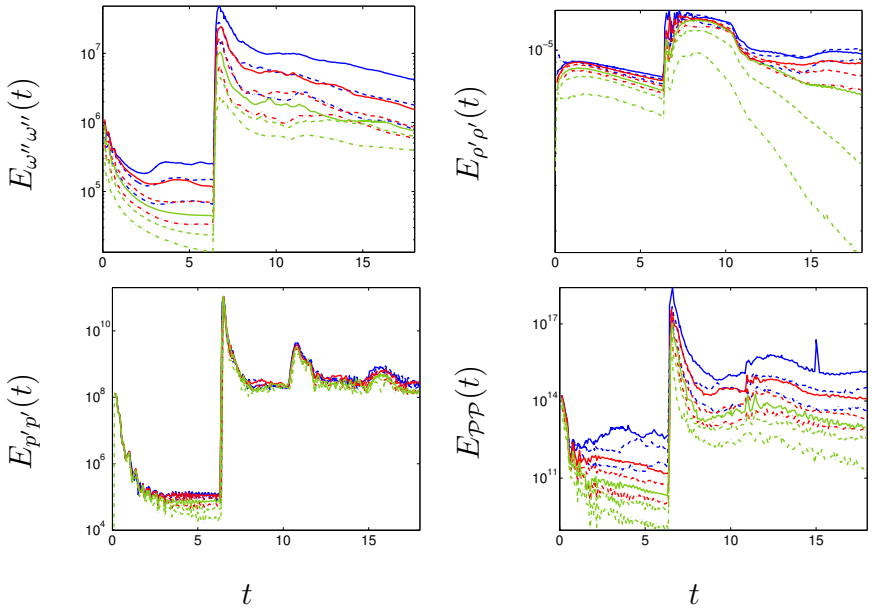

Fig. 15. Comparison of the time-evolution of the turbulent enstrophy, density variance, pressure variance and baroclinic vorticity production variance, $E_{\omega''\omega''}(t)$, $E_{\rho'\rho'}(t)$, $E_{p'p'}(t)$ and $E_{\mathcal{P}\mathcal{P}}(t)$, when the order and resolution are varied. See Fig. 8 for the legend.

5.5 The probability distribution functions

A novel quantitative measure of the effects of order and resolution on primitive, fluctuating and derived scalar fields represented on the computational grid is provided by the probability distribution. The probability with which a particular value of a scalar field occurs at a particular time during the evolution of the instability can be quantified using the probability distribution function (PDF) $P(\phi, t)$. Consider the field $\phi(x, y, t)$ within the mixing layer $(x, y) \in [\ell_s, \ell_b] \times [0, L_y]$ discretized by $N_x \times N_y$ points. Divide the range $[\min(\phi), \max(\phi)]$

into $M = \sqrt{N_x N_y}/2$ (an integer) equal bins $\Delta\phi \equiv [\max(\phi) - \min(\phi)]/M$. Each discrete value of $\phi(x_i, y_j, t)$ is distributed in the bins, yielding the frequency N_k, so that the PDF is defined as

$$P_k(\phi, t) = \frac{N_k}{\Delta\phi \, N_x \, N_y}, \tag{16}$$

satisfying $\sum_{k=1}^{M} P_k(\phi, t)\Delta\phi = 1$ ($\int_{-\infty}^{\infty} P(\phi, t)\mathrm{d}\phi = 1$ in the continuum limit).

At 6 ms, the density PDF $P(\rho)$ in Fig. 16 has peaks corresponding to the density of air(acetone) (left peak) and SF_6 (right peak). As the order and resolution increase (with a decrease in numerical dissipation and numerically-induced mixing), the magnitude of the PDF between the peaks decreases. At 7 ms, the PDF has a smoother peak in the SF_6, corresponding to the reflected rarefaction creating a wider range of scales, whereas the peak in the air(acetone) is compressed by the passage of the transmitted shock, creating a narrower range of scales. The PDF at 7 ms exhibits greater sensitivity to the order and resolution. By contrast, the layer is nearly uniformly mixed at 18 ms and $P(\rho)$ shows less sensitivity at high order and resolution. The pressure PDF $P(p)$ at 6 ms has a single peak corresponding to the pressure following shock passage. At 7 ms, the pressure peak is broadened by the reflected rarefaction, and further narrows at 18 ms. Higher-order higher-resolution PDFs have longer tails, indicating the presence of additional smaller scales.

Figure 16 also shows the PDFs of the components of the density and pressure gradients in the streamwise direction $P(\partial\rho/\partial x)$ and $P(\partial p/\partial x)$, which exhibit increased sensitivity to the order and resolution. Higher-order higher-resolution simulations exhibit a wider range of scales, reflected in broader PDFs. The components of the density and pressure gradients form the baroclinic vorticity production $\mathcal{P}$: higher-order higher-resolution simulations yield larger values of the baroclinic vorticity production, as shown by the PDF of $\mathcal{P}$ in Fig. 18. The PDFs of the density and pressure gradients in the spanwise direction are similar to those in the streamwise direction and are not shown.

At 6 ms the PDF of the streamwise velocity fluctuation $P(u'')$ in Fig. 17 exhibits several peaks corresponding to the different roll-up regions. At 7 ms, two peaks corresponding to the rapid expansion (in both directions) of the mixing layer form. A single symmetric peak at late times corresponds to a decaying mixing layer. All of the simulations capture the shapes and values of the peaks, with higher-order higher-resolution simulations exhibiting wider PDFs corresponding to larger positive and negative values of the fluctuations. The PDF of the spanwise velocity fluctuation $P(v'')$ exhibits a single slightly asymmetric peak at 6 and 7 ms (corresponding to the roll-ups) and becomes symmetric at 18 ms. As in the case of the streamwise component, all of the simulations capture the peak and have similar widths, with higher-

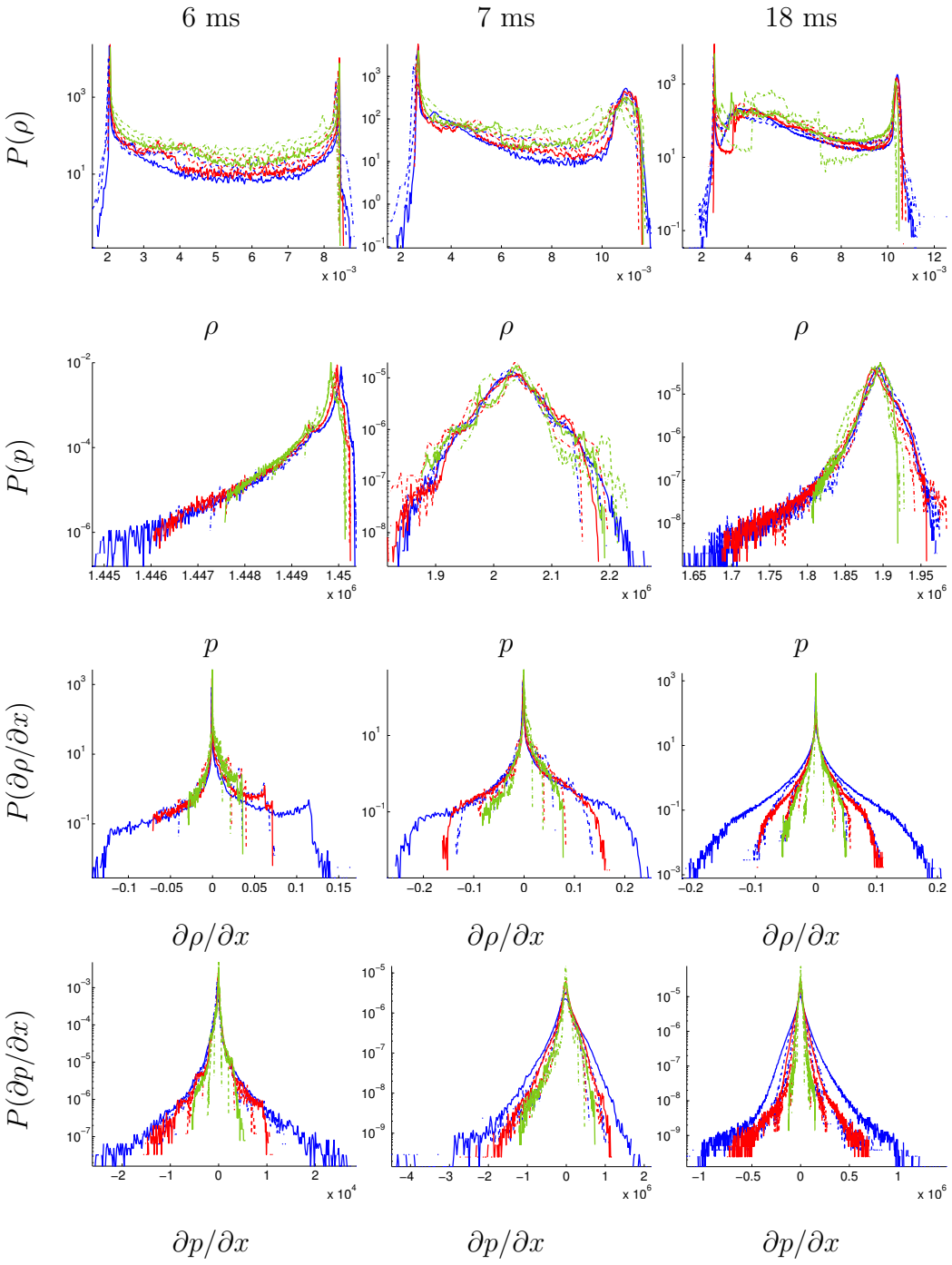

Fig. 16. Comparison of the PDFs of the density and pressure, $P(\rho)$ and $P(p)$, and of the components of the density and pressure gradients in the streamwise direction, $P(\partial\rho/\partial x)$ and $P(\partial p/\partial x)$, at 6, 7 and 18 ms when the order and the grid resolution are varied. See Fig. 8 for the legend.

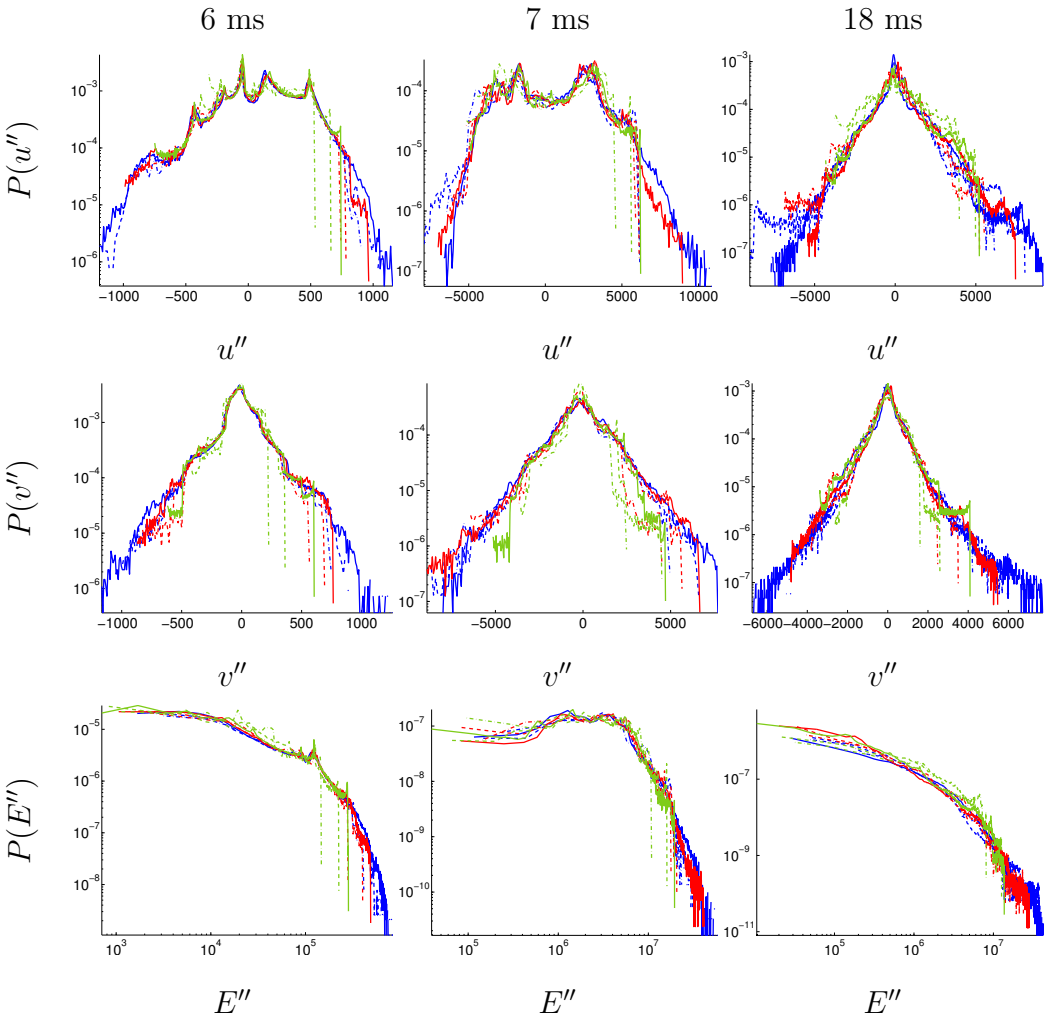

Fig. 17. Comparison of the PDFs of the streamwise and spanwise velocity fluctuation $P(u'')$ and $P(v'')$ and fluctuating kinetic energy $P(E'')$ at 6, 7 and 18 ms when the order and resolution are varied. See Fig. 8 for the legend.

order higher-resolution PDFs exhibiting additional scales at larger values of the fluctuations. The PDF of the fluctuating kinetic energy per unit mass $P(E'')$, where $E'' = (u''^2 + v''^2)/2$, indicates that all simulations have similar distributions at small values. The lower-order lower-resolution PDFs rapidly decrease, corresponding to numerically damped smaller-scale fluctuations.

The PDF of the vorticity $P(\omega)$ in Fig. 18 has a single symmetric peak at all times. Higher-order higher-resolution $P(\omega)$ have broader peaks, consistent with more localized and larger vorticity. The peak is particularly broad following reshock at 7 ms. As shown in Fig. 6, the higher-order simulations exhibit additional structures on the roll-up that contribute to increased vorticity deposition on the interface. The differences in the $P(\omega)$ among orders and resolutions decrease at late times. The PDF of the baroclinic vorticity production $P(\mathcal{P})$ is also shown (with the values on the horizontal axis on

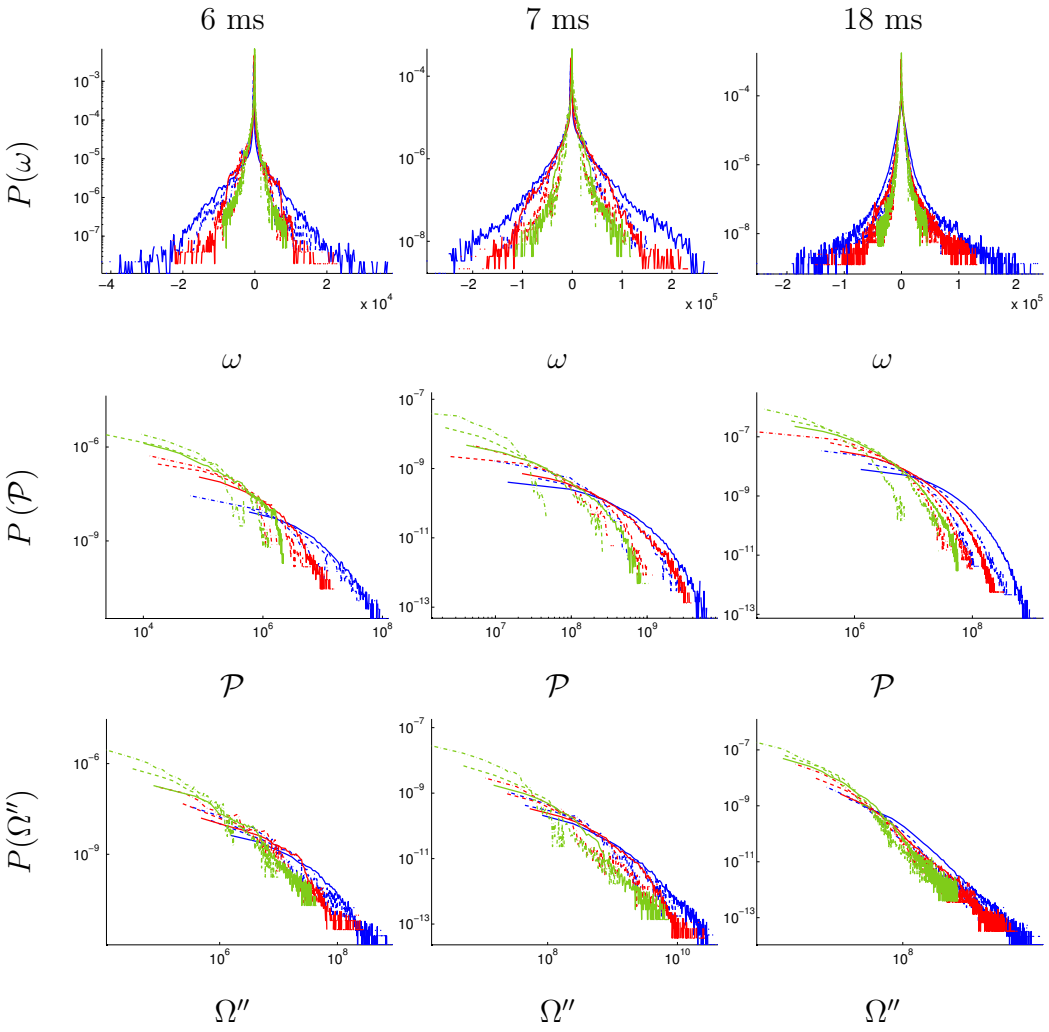

Fig. 18. Comparison of the PDFs of the vorticity $P(\omega)$, baroclinic vorticity production $P(\mathcal{P})$, and fluctuating enstrophy $P(\Omega'')$ at 6, 7 and 18 ms when the order and resolution are varied. See Fig. 8 for the legend.

a logarithmic scale), indicating that lower-order lower-resolution simulations have higher probability of production at smaller values. By contrast, higher-order higher-resolution simulations exhibit larger values of the PDFs, which can be explained by the broader PDFs of the density and pressure gradient components shown in Fig. 16. The PDFs of the fluctuating enstrophy per unit mass $P(\Omega'')$, where $\Omega'' = \omega''^2/2$, from lower-order lower-resolution simulations exhibit a higher probability of smaller values of the enstrophy, whereas higher-order higher-resolution simulations exhibit a broader range of values.

6 Quantification of numerical dissipation: numerical turbulent kinetic energy and enstrophy production/dissipation rates, Reynolds numbers and viscosity

The dependence of the results in Secs. 3–5 on the order and resolution is interpreted here by computing the implicit numerical dissipation of the WENO method using the numerical turbulent kinetic energy and enstrophy production/dissipation rates, Reynolds numbers and viscosity.

6.1 The numerical turbulent kinetic energy and enstrophy production/dissipation rates

Here the numerical turbulent kinetic energy production/dissipation rate $\widetilde{\epsilon''}(t)$ is computed from the simulations using two different expressions. In the case of an Euler simulation of the reshocked Richtmyer-Meshkov instability, the turbulent kinetic energy is dissipated by numerical mechanisms after the shock has passed through the interface. The interaction of the shock with the mixing layer imparts kinetic energy into the flow (production). As $\widetilde{\epsilon''}$ is not uniquely defined, two independent expressions for this quantity are used and compared. The numerical turbulent enstrophy production/dissipation rate $\widetilde{\epsilon''_\omega}(t)$ can also be computed from the simulations. As in the case of the turbulent kinetic energy, the turbulent enstrophy is dissipated by numerical mechanisms after the shock has passed through the interface.

The first method to quantify $\widetilde{\epsilon''}(t)$ over the flow evolution entails computing the negative of the time-rate-of-change of the turbulent kinetic energy [41],

$$\widetilde{\epsilon''}(t) = -\frac{\mathrm{d}E(t)}{\mathrm{d}t}\,. \tag{17}$$

Another estimate of $\widetilde{\epsilon''}$ is given by turbulent transport phenomenology [42]

$$\widetilde{\epsilon''}(t) = E(t)\,\sqrt{2\,E_{\omega''\omega''}(t)}\,, \tag{18}$$

where $E_{\omega''\omega''}(t) = \widetilde{\omega''^2}/2$ is the turbulent enstrophy per unit mass. The negative of the time-rate-of-change of $\widetilde{\epsilon''_\omega}(t)$ provides a direct measure of the production/dissipation rate:

$$\widetilde{\epsilon''_\omega}(t) = -\frac{\mathrm{d}E_{\omega''\omega''}(t)}{\mathrm{d}t}\,. \tag{19}$$

Both formulations of $\widetilde{\epsilon''}$ shown in Fig. 19 are qualitatively similar. In particular, $\widetilde{\epsilon''}$ peaks following the passage of the initial incident shock and then decreases.

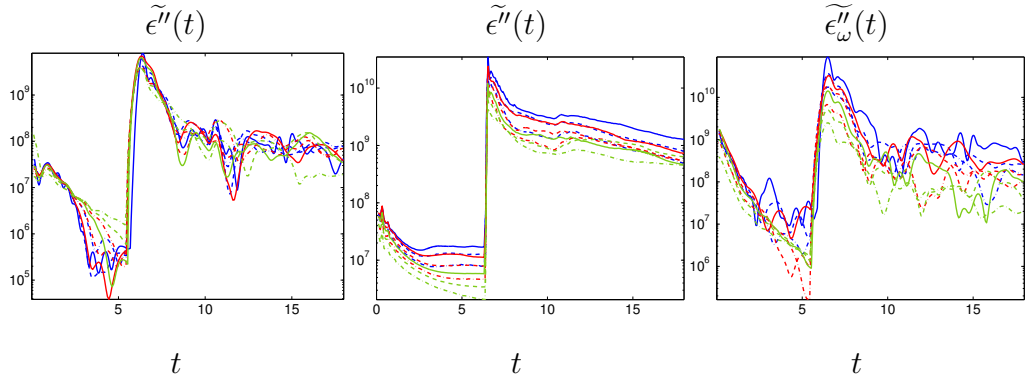

Fig. 19. Comparison of the time-evolution of the numerical turbulent kinetic energy production/dissipation rate $\widetilde{\epsilon''}(t)$, computed using Eqs. (17) and (18), respectively, when the order and resolution are varied; $\widetilde{\epsilon''}(t)$ is computed from Eq. (17) by taking the five-point average of $E(t)$ prior to differentiation. Also shown is a comparison of the time-evolution of the numerical turbulent enstrophy production/dissipation rate $\widetilde{\epsilon''_\omega}(t)$, when the order and resolution are varied. See Fig. 8 for the legend.

Reshock rapidly deposits energy into the layer and sharply increases $\widetilde{\epsilon''}$ by four to five orders of magnitude. Following reshock, $\widetilde{\epsilon''}$ decreases rapidly. The WENO9F simulation yields the largest $\widetilde{\epsilon''}$ based on Eq. (18), as the increased kinetic energy of higher-order higher-resolution simulations corresponds to larger $\widetilde{\epsilon''}$. Similarly, the WENO3C simulation has the smallest $\widetilde{\epsilon''}$, as the corresponding kinetic energy content is lower. While both values of $\widetilde{\epsilon''}$ are affected by the arrival of the reflected rarefaction at ≈ 11 ms, that based on Eq. (17) is affected more strongly. The interaction of the shock with the interface (or mixing layer) deposits vorticity and, therefore, increases $E_{\omega''\omega''}(t)$ and $\widetilde{\epsilon''_\omega}(t)$. The turbulent enstrophy production/dissipation rate $\widetilde{\epsilon''_\omega}(t)$ in Fig. 19 exhibits a qualitative behavior similar to that of $\widetilde{\epsilon''}(t)$ in Fig. 19. Reshock further increases $\widetilde{\epsilon''_\omega}$ by three to four orders of magnitude, followed by a rapid decrease. The WENO9 $\widetilde{\epsilon''_\omega}$ are the largest, indicating that the enstrophy is produced and dissipated at a faster rate in higher-order higher-resolution simulations.

6.2 The numerical Reynolds numbers

Another quantification of implicit dissipation is given by computing a numerical Reynolds number. In the present simulations based on the Euler equations, there is no unique definition of the Reynolds number, so that two different expressions are compared. The first was used in blast wave simulations [43]

$$\mathrm{Re}_h(t) = \left[\frac{h(t)}{\Delta x}\right]^{4/3}, \tag{20}$$

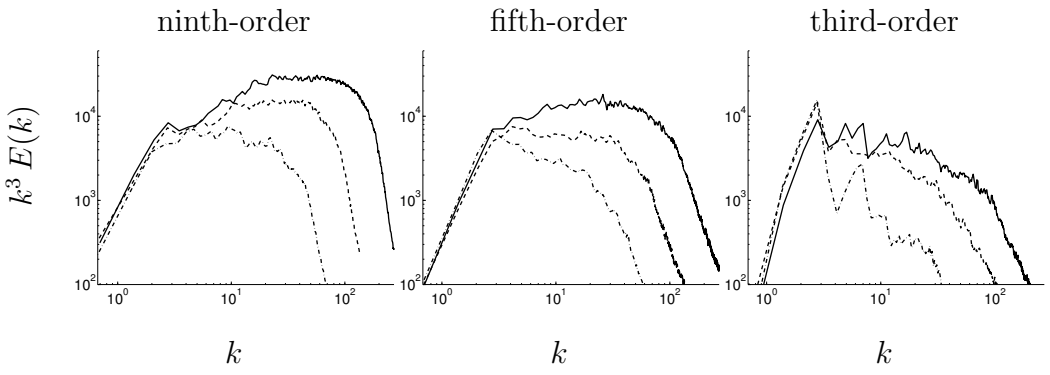

Fig. 20. Comparison of the compensated turbulent kinetic energy spectra $k^3E(k)$ at 18 ms when the order and resolution are varied. Quantities obtained on the fine, medium and coarse grids are shown using a solid, dashed and dash-dot line, respectively.

where $h(t)$ is the mixing layer width and Δx is the grid spacing. This Reynolds number is based on the largest scale in the flow given by $h(t)$. Note that each doubling of the resolution contributes to an increase of $2^{4/3} \approx 2.5$ in Re_h. A second definition of the Reynolds number was used in two-mode Richtmyer-Meshkov instability simulations [10]:

$$\mathrm{Re}_\ell(t) = \left[\frac{\ell(t)}{\ell_d}\right]^{4/3}, \tag{21}$$

where

$$\ell(t) = \frac{3\,\pi}{4}\,\frac{\int_0^{k_\mathrm{max}} \frac{E(k,t)}{k}\,\mathrm{d}k}{\int_0^{k_\mathrm{max}} E(k,t)\,\mathrm{d}k} \tag{22}$$

is the integral length scale [44] and $\ell_d = 2\pi/k_d$ is the Kolmogorov length scale. The Kolmogorov wavenumber can be estimated as $k_d = 50k_\nu$ [45], where the dissipation wavenumber k_ν is the value of k at which the turbulent kinetic energy spectrum $E(k,t)$ begins to steepen from the -3 law expected for two-dimensional turbulent flows exhibiting an inertial subrange [4]. The Reynolds number given by Eq. (21) is based on $\ell(t)$, which is related to the energy content of the largest scales. Thus, the Reynolds numbers behave differently as they are based on different length scales. Both Reynolds numbers were used in three-dimensional simulations: as the estimates are obtained from the range of scales along a single spatial direction, these definitions are also appropriate for the present simulations.

First, the values of k_ν are determined by plotting the compensated turbulent kinetic energy spectra $k^3E(k)$ shown in Fig. 20, where the WENO9, WENO5 and WENO3 results are shown for each of the grid resolutions considered: k_ν corresponds to the wavenumber where the spectrum is no longer horizontal, which is estimated visually. The compensated spectra are shown at 18 ms, but k_ν changes very little when the spectra are considered at $6, 7$ and 12 ms

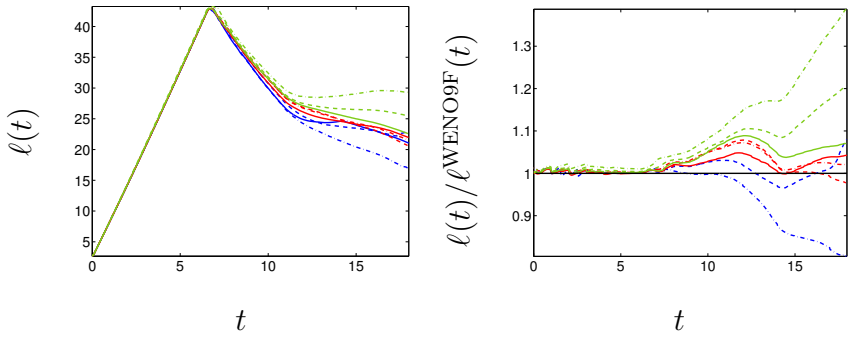

Fig. 21. Comparison of the time-evolution of the integral length scale $\ell(t)$ when the order and resolution are varied (left). The integral length scales normalized by that from the WENO9F simulation is also shown (right). See Fig. 8 for the legend.

instead. As the resolution increases for a given order, the compensated spectra broaden and increase in magnitude. At small k, the compensated spectra are nearly the same. As the order increases for a given resolution, the compensated spectra become flatter and also broaden.

Prior to reshock, the integral length scale $\ell(t)$ in Fig. 21 increases and very weakly depends on the order and resolution. Following reshock $\ell(t)$ decreases with increased sensitivity to the order and resolution. Higher-order higher-resolution simulations yield smaller $\ell(t)$. The agreement in $\ell(t)$ prior to reshock indicates similar energy content in the largest scales. The arrival of the reflected rarefaction at ≈ 11 ms deposits energy, which slows the decrease of $\ell(t)$. Up to the arrival of the reflected rarefaction, the $\ell(t)$ are within 10% of one another. Note that $\ell(t) > h(t)$ up to reshock. Also, $\ell(t)$ grows linearly prior to reshock and decays linearly after reshock, prior to the arrival of the reflected rarefaction.

Both numerical Reynolds numbers in Fig. 22 increase prior to reshock. However, the $\mathrm{Re}_h(t)$ are grouped by the resolution (as shown by the ratio of the Reynolds numbers), while the Re_ℓ are grouped by the order and resolution. After reshock, the Reynolds numbers behave entirely differently: $\mathrm{Re}_h(t)$ decreases due to the compression of the mixing layer caused by reshock, while $\mathrm{Re}_\ell(t)$ peaks at reshock due to the large energy deposition during reshock. Following reshock, $\mathrm{Re}_h(t)$ increases while $\mathrm{Re}_\ell(t)$ decreases. Note that $\mathrm{Re}_\ell(t)$ peaks at a value $\sim 1.1 \times 10^6$ at reshock in the WENO9F simulation, with the peaks from all other simulations considerably lower.

6.3 The numerical viscosity

Assuming a correspondence between molecular and numerical dissipation, a numerical viscosity can be dimensionally computed from the Kolmogorov

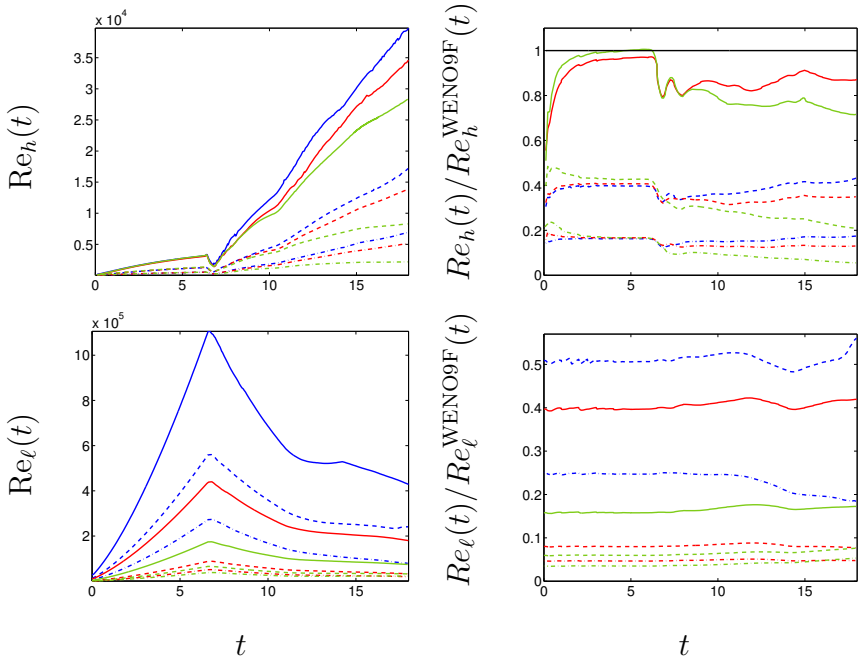

Fig. 22. Comparison of the time-evolution of the numerical Reynolds numbers $\mathrm{Re}_h(t)$ and $\mathrm{Re}_\ell(t)$ when the order and resolution are varied (left column). The numerical Reynolds numbers normalized by that from WENO9F simulation are also shown (right column). See Fig. 8 for the legend.

length scale and the turbulent kinetic energy production/dissipation rate,

$$\nu_{\mathrm{num}}(t) = \ell_d^{4/3}\, \widetilde{\epsilon''}(t)^{1/3}\,. \tag{23}$$

Two numerical viscosities can be computed using $\widetilde{\epsilon''}(t)$ given by Eqs. (17) and (18). This determination of $\nu_{\mathrm{num}}(t)$ is different from that in [13], where one-dimensional solutions of the Euler equations were 'matched' to converged solutions of the Navier-Stokes equations with different Reynolds numbers using the fifth-order WENO method. The numerical viscosity was then estimated to be similar to the physical viscosity of the matched solutions.

Figure 22 shows the numerical viscosities $\nu_{\mathrm{num}}(t)$ as the order and resolution are varied, using $\widetilde{\epsilon''}(t)$ given by Eqs. (17) and (18). Increasing the order and resolution corresponds to simulations with decreasing numerical dissipation. The numerical viscosity increases at reshock, corresponding to additional energy deposition into the mixing layer, followed by a decrease at later times. The extreme cases correspond to a difference of one order of magnitude or greater in the value of $\nu_{\mathrm{num}}(t)$ at any given time: the ratios of the numerical viscosities to that from the WENO9F simulation indicate that increasing the order from fifth to ninth constitutes a $\approx$ 2.5-fold decrease in $\nu_{\mathrm{num}}(t)$, while doubling the resolution results in only a $\approx$ 1.5-fold decrease. Similar trends are found when the order is changed from third to fifth and the resolution is doubled. These findings are also generally consistent with those in [13].

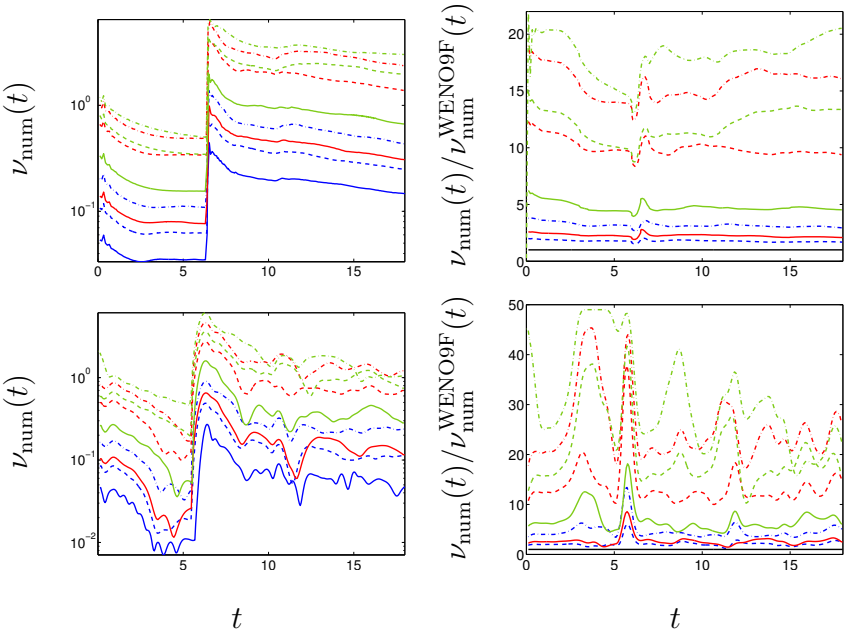

Fig. 23. Comparison of the time-evolution of the numerical viscosity $\nu_{\rm num}(t)$ obtained using the turbulent kinetic energy production/dissipation rate of Eq. (18) (top left) and Eq. (17) (bottom left) when the order and resolution are varied. The numerical viscosity computed using $\widetilde{\epsilon''}(t)$ given by Eq. (17) shows additional noise. The numerical viscosities normalized by that from the WENO9F simulation are also shown (right column). See Fig. 8 for the legend.

7 Discussion and conclusions

Simulations of the two-dimensional reshocked single-mode Richtmyer-Meshkov instability were performed using third-, fifth- and ninth-order WENO flux reconstruction and uniform spatial grid resolutions of 128, 256 and 512 points per initial perturbation wavelength to investigate the dependence of the following quantities on the order and resolution: (1) the density, vorticity, simulated density Schlieren, and the baroclinic vorticity production fields; (2) the mixing layer width; (3) the circulation; (4) mixing profiles; (5) production and mixing fractions; (6) energy spectra; (7) statistics; (8) probability distribution functions (PDFs); (9) the turbulent kinetic energy and turbulent enstrophy production/dissipation rates; (10) numerical Reynolds numbers, and; (11) the numerical viscosity. To our knowledge, *this is the first systematic investigation of the predictions of the WENO method applied to such a broad array of quantities as a function of order and resolution in the case of the reshocked Richtmyer-Meshkov instability.* This broad range of quantities includes large-scale dominated quantities (e.g., the mixing layer width), primitive fields (e.g., the density), derived fields (e.g., the vorticity and the density and pressure gradients), spatially-averaged quantities (mixing profiles), quantities characterizing the distribution of fluctuations across scales (spectra), global quantities

(statistics), and quantities characterizing the range of values (PDFs).

The density, vorticity, baroclinic vorticity production, and simulated density Schlieren fields were compared before and after reshock. Prior to reshock, the higher-order higher-resolution densities exhibited additional finer-scale structure in the roll-up. The formation of this additional structure was understood by considering the vorticity and baroclinic vorticity production fields. The higher-order higher-resolution vorticities exhibited strong localized cores surrounded by a vortex bilayer with vorticity of opposite sign, followed by late-time fragmentation of the roll-up. Such fragmentation does not occur in the lower-order lower-resolution simulations. The simulated density Schlieren fields were used to visualize the transmitted and reflected waves at reshock. The lower-order lower-resolution Schlierens exhibited thicker waves, while the higher-order higher-resolution Schlierens exhibited sharper small-scale waves. Numerical dissipation damps the high-frequency components, smearing the waves in the lower-order lower-resolution simulations. The higher-order higher-resolution densities exhibited symmetry breaking and the formation of complex small-scale structures; similarly, the vorticities fragmented and formed localized cores. In contrast, the lower-order lower-resolution densities exhibited symmetric large-scale structures and vorticities with more diffuse cores.

Prior to reshock, the mixing layer width $h(t)$ exhibited little dependence on the order and resolution. However, following reshock and particularly following the arrival of the reflected rarefaction, the $h(t)$ were significantly different among the simulations, which can be attributed to the implicit numerical dissipation suppressing the formation of small-scale structures in low-order low-resolution simulations and damping velocity fluctuations (particularly the streamwise fluctuations associated with the mixing layer growth along the shock propagation direction). Therefore, increased numerical diffusion results in smaller $h(t)$. As the order and resolution increase, the differences between the widths decrease, suggesting a trend toward numerical 'convergence'. In addition, smaller baroclinic circulation deposition during a wave-interface interaction occurs in simulations with large numerical diffusion compared to the higher-order higher-resolution simulations, which exhibit fragmentation and more small-scale structure. The energy deposited into the layer by reshock generates small-scale structures, which explains the differences in widths as less energy is deposited in low-order low-resolution simulations.

The mixing profiles showed different degrees of sensitivity to the order and resolution. Prior to and immediately following reshock, the differences are due to the numerical diffusion. The differences in the mixing profiles at late times are due to significant differences in the underlying flow structure. Higher-order higher-resolution simulations exhibited fragmented structure with localized mixed regions, resulting in more pronounced localized peaks in the profiles. Instead, lower-order lower-resolution simulations exhibited more coherent large-

scale structures, resulting in fewer peaks spread over a larger portion of the layer. As a result, the mole fraction profile $\overline{X}$ had similar values prior to and immediately following reshock as the order and resolution increased. However, the averaged product mole fraction profile $\overline{X}_p$ exhibited differences prior to and following reshock.

The production and mixing fractions significantly depend on the order and resolution, which is related to the small-scale structures within the mixing layer at late times following reshock. Low-order low-resolution simulations with increased dissipation resulted in greater numerical mixing as measured by the production mixing fraction P_t before and after reshock. High-order high-resolution simulations with less numerical dissipation had smaller P_t. Prior to reshock, low-order low-resolution simulations had larger mixing fractions Ξ, consistent with increased mixing due to the larger numerical dissipation. However, following reshock, Ξ was not very sensitive to the order and resolution. Similar mechanisms also explain the behavior of the mixing fraction Θ, which exhibited stronger sensitivity than Ξ to order and resolution.

The energy spectra exhibited different degrees of sensitivity to the order and resolution. The large-scale kinetic energy and density variance spectra are insensitive to the order and resolution, while the remaining spectra are highly sensitive to both order and resolution over all scales. Most of the sensitivity is exhibited at the intermediate and small scales. The turbulent kinetic energy spectrum $E(k,t)$ exhibited little sensitivity to the order and resolution, whereas the turbulent enstrophy spectrum $E_{\omega''\omega''}(k,t)$ exhibited significantly more sensitivity, with higher-order higher-resolution simulations having larger values over a broader range of scales. The density variance spectrum $E_{\rho'\rho'}(k,t)$ exhibited sensitivity to the order and resolution at large k. The pressure variance spectrum $E_{p'p'}(k,t)$ exhibited sensitivity to order and resolution, both at small and large k. Higher-order higher-resolution simulations baroclinic vorticity production variance spectra $E_{\mathcal{P}\mathcal{P}}(k,t)$ remained large over a larger extent of scales and were larger in magnitude. By contrast, lower-order lower-resolution spectra decayed rapidly and had smaller values. The WENO9F density and pressure variance spectra have an apparent inertial subrange over slightly more than a decade and over approximately one decade in wavenumbers, respectively. The numerical dissipation of lower-order lower-resolution simulations rapidly damps the small-scale fluctuations in the flow. *Spectra corresponding to derived quantities (i.e., quantities depending on spatial derivatives such as the vorticity and baroclinic vorticity production) are highly sensitive to the order and resolution.*

The statistics also exhibited sensitivity to order and resolution similar to those exhibited by the corresponding energy spectra. The turbulent kinetic energy $E(t)$ exhibited small differences prior to and following reshock, with the differences prior to reshock due to the complex structure in the roll-up. A more

significant difference was observed in the spanwise turbulent kinetic energy $E_{v''v''}(t)$ prior to and following reshock due to the spanwise fluctuations excited by the roll-up and the complex structures in the flow. The turbulent enstrophy $E_{\omega''\omega''}(t)$ and baroclinic vorticity production variance $E_{\mathcal{P}\mathcal{P}}(t)$ exhibited significant variation over all times. The density and pressure variance $E_{\rho'\rho'}(t)$ and $E_{p'p'}(t)$ also exhibited variations prior to and following reshock.

Probability distribution functions (PDFs) were considered to investigate the distribution of values of various primitive, fluctuating and derived scalar fields in the flow, and it was found that *while the different simulations give similar predictions of mean values, quantities depending on smaller-scale structures or with extreme values differ, i.e., the tails of the PDFs corresponding to the extreme values are broader or narrower, depending on the relative numerical dissipation.* Specifically, higher-order higher-resolution fluctuating field PDFs are broader, corresponding to a wider range of values. Similarly, higher-order higher-resolution field gradient PDFs are wider, corresponding to larger absolute values of the gradients. As a result, higher-order higher-resolution vorticity and baroclinic vorticity production fields have increased ranges of values. *This has important implications for using numerical simulation data to assess turbulent transport or subgrid-scale models, as lower-order lower-resolution simulations are excessively diffusive and strongly limit the range of values of quantities supported on a given computational grid.*

The sensitivity exhibited by the quantities considered in this study was largely explained by the different implicit numerical dissipation associated with each order and resolution. The turbulent kinetic energy production/dissipation rate $\widetilde{\epsilon''}(t)$ was computed using two expressions, which were shown to be qualitatively similar. Larger turbulent kinetic energy and turbulent enstrophy production/dissipation are associated with higher-order higher-resolution simulations, as the kinetic energy and enstrophy in these simulations is larger. The trends for the turbulent enstrophy production/dissipation rate $\widetilde{\epsilon''_\omega}(t)$ were similar to those for $\widetilde{\epsilon''}(t)$. The numerical viscosity $\nu_{\text{num}}(t)$ computed using $\widetilde{\epsilon''}(t)$ and a dissipation length scale confirmed that higher-order higher-resolution simulations have reduced numerical dissipation. Doubling the resolution corresponds to an ≈ 1.5-fold decrease in $\nu_{\text{num}}(t)$, while approximately doubling the order corresponds to an ≈ 2.5-fold decrease. Therefore, *for the complex shock-driven flow considered here, approximately doubling the order yields a larger decrease in the numerical dissipation than doubling the resolution. Furthermore, at least a ninth-order WENO method is recommended if either explicit molecular dissipation and diffusion, or explicit subgrid-scale or Reynolds-averaged Navier-Stokes models are included in such simulations.*

Two numerical Reynolds numbers were compared: the first, $\text{Re}_h(t)$, is based on the range of scales between the grid resolution Δx and the mixing layer width $h(t)$, while the second, $\text{Re}_\ell(t)$, is based on the range of scales between

	Coarse (128)	Medium (256)	Fine (512)
Ninth-order	0.4	2.3	20.7
Fifth-order	0.2	1.0	9.5
Third-order	0.17	0.8	7.1

Table 2
Ratio of CPU times for advancing the simulations by $\Delta t = 0.1$ ms compared with the time needed for the fifth-order simulation at medium resolution.

the integral length scale $\ell(t)$ and the numerical analog of the Kolmogorov dissipation length scale ℓ_d; $\mathrm{Re}_h(t)$ is associated with the largest scales present in the flow, while $\mathrm{Re}_\ell(t)$ is associated with turbulent quantities. The WENO9F simulation attains the largest Reynolds numbers, as this simulation has the least numerical dissipation. The temporal decay of Re_ℓ is consistent with a decaying turbulent flow following reshock of the mixing layer, where the decay mechanism is due to the numerical dissipation. *Larger numerical Reynolds numbers are attained in high-order high-resolution simulations.*

Finally, a note regarding the relative computational cost of the simulations presented here, which were conducted on the Blue Pacific computer at the Lawrence Livermore National Laboratory. For each simulation, 32 nodes were used with a total of 128 processors. The CPU times required to advance the simulation between 12.5 and 12.6 ms were compared to the time required for the WENO5M simulation. The ratios of the CPU times to that for the WENO5M simulation are shown in Table 2, which indicates that increasing the order requires twice the computational time, whereas doubling the resolution requires five to eight times more computational time. These findings are generally consistent with [11].

The reduced numerical dissipation in formally high-order methods, coupled with consideration of the computational cost, suggests that such methods are well-suited for simulating complex multi-scale flows with shocks. Lower dissipation simulations preserve additional small-scale structures and provide a more complete representation of the flow dynamics. Low-order representations of complex flow physics are considerably different than high-order representations and, in general, a broad range of quantities should be considered to differentiate between the predictions of different numerical methods. The use of formally higher-order methods is also more computationally efficient than increasing the grid resolution for the two-dimensional Richtmyer-Meshkov instability, leading to a significant advantage in *multi-dimensional* simulations of such flows. While definitive experimental data corresponding to the quantities considered in the present study is required to assess the simulation predictions, higher-order higher-resolution simulations likely provide higher fidelity data. The analysis presented here is currently being applied to a three-dimensional reshocked multi-mode Richtmyer-Meshkov instability-induced flow.

Acknowledgments

The authors thank Dr. Daniel I. Meiron for useful discussions. Marco Latini acknowledges support from the Air Force Office of Scientific Research (AFOSR) through the National Defense Science and Engineering Graduate (NDSEG) Fellowship and the Caltech Accelerated Strategic Computing (ASC) Center. Wai Sun Don acknowledges support by the DOE under contract number DE-FG02-98ER25346 and by the AFOSR under contract number FA9550-05-1-0123. This work was also performed under the auspices of the U.S. Department of Energy by the University of California, Lawrence Livermore National Laboratory under contract No. W-7405-Eng-48.

References

[1] D. Balsara, C.-W. Shu, Monotonicity preserving weighted essentially non-oscillatory schemes with increasingly high order of accuracy, J. Comput. Phys. 160 (2000) 405–452.

[2] M. Latini, O. Schilling, W. S. Don, High-resolution simulations and modeling of reshocked single-mode Richtmyer-Meshkov instability. I. Comparison to experimental data and to amplitude growth model predictions, Phys. FluidsSubmitted.

[3] B. D. Collins, J. W. Jacobs, PLIF flow visualization and measurements of the Richtmyer-Meshkov instability of an air/SF_6 interface, J. Fluid Mech. 464 (2002) 113–136.

[4] O. Schilling, M. Latini, W. S. Don, High-resolution simulations and modeling of reshocked single-mode Richtmyer-Meshkov instability. II. Physics of reshock and mixing, Phys. FluidsSubmitted.

[5] G. Tryggvason, Numerical simulations of the Rayleigh-Taylor instability, J. Comput. Phys. 75 (1988) 253–282.

[6] X. He, S. Chen, R. Zhang, A lattice Boltzmann scheme for incompressible multiphase flow and its application in simulation of Rayleigh-Taylor instability, J. Comput. Phys. 152 (1999) 642–663.

[7] G. Dimonte, D. L. Youngs, A. Dimits, S. Weber, M. Marinak, S. Wunsch, C. Garasi, A. Robinson, M. J. Andrews, P. Ramaprabhu, A. C. Calder, B. Fryxell, J. Biello, L. Dursi, P. MacNeice, K. Olson, P. Ricker, R. Rosner, F. Timmes, H. Tufo, Y.-N. Young, M. Zingale, A comparative study of the turbulent Rayleigh-Taylor instability using high-resolution three-dimensional numerical simulations: The Alpha-Group collaboration, Phys. Fluids 16 (2004) 1668–1693.

[8] R. L. Holmes, J. W. Grove, D. H. Sharp, Numerical investigation of Richtmyer-Meshkov instability using front-tracking, J. Fluid Mech. 301 (1995) 51–64.

[9] R. L. Holmes, G. Dimonte, B. Fryxell, M. L. Gittings, J. W. Grove, M. Schneider, D. H. Sharp, A. L. Velikovich, R. P. Weaver, Q. Zhang, Richtmyer-Meshkov instability growth: experiment, simulation and theory, J. Fluid Mech. 389 (1999) 55–77.

[10] R. H. Cohen, W. P. Dannevik, A. M. Dimits, D. E. Eliason, A. A. Mirin, Y. Zhou, D. H. Porter, P. R. Woodward, Three-dimensional simulation of a Richtmyer-Meshkov instability with a two-scale initial perturbation, Phys. Fluids 14 (2002) 3692–3709.

[11] J. Shi, Y.-T. Zhang, C.-W. Shu, Resolution of high order WENO schemes for complicated flow structures, J. Comput. Phys. 186 (2003) 690–696.

[12] A. W. Cook, W. H. Cabot, J. A. Greenough, A High-Order Method for Shock-Induced Mixing, Tech. Rep. UCRL-JC-144109, Lawrence Livermore National Laboratory (2001).

[13] Y.-T. Zhang, J. Shi, C.-W. Shu, Y. Zhou, Numerical viscosity and resolution of high-order weighted essentially nonoscillatory schemes for compressible flows with high Reynolds numbers, Phys. Rev. E 68 (2003) 046709–1–046709–16.

[14] P. L. Roe, Approximate Riemann solvers, parameter vectors, and difference schemes, J. Comput. Phys. 43 (1981) 357–372.

[15] J. P. Boris, F. F. Grinstein, E. S. Oran, R. L. Kolbe, New insights into large eddy simulation, Fluid Dyn. Res. 10 (1992) 199–228.

[16] D. Drikakis, Embedded turbulence model in numerical methods for hyperbolic conservation laws, Int. J. Num. Meth. Fluids 39 (2002) 763–781.

[17] D. Drikakis, Advances in turbulent flow computations using high-resolution methods, Prog. Aero. Sci. 39 (2003) 405–424.

[18] D. Drikakis, F. Grinstein, D. Youngs, On the computation of instabilities and symmetry-breaking in fluid mechanics, Prog. Aero. Sci. 41 (2005) 609–641.

[19] H. O. Kreiss, J. Oliger, Comparison of accurate methods for integration of hyperbolic equations, Tellus 24 (1972) 199–215.

[20] L. Jameson, High order schemes for resolving waves: number of points per wavelength, J. Sci. Comput. 15 (2000) 417–439.

[21] A. Marquina, P. Mulet, A flux-split algorithm applied to conservative models for multicomponent compressible flows, J. Comput. Phys 185 (2003) 120–138.

[22] D. J. Hill, D. I. Pullin, Hybrid tuned center-difference-WENO method for large eddy simulations in the presence of strong shocks, J. Comput. Phys. 194 (2004) 435–450.

[23] A. K. Henrick, T. D. Aslam, J. M. Powers, Powers, mapped weighted essentially non-oscillatory schemes: achieving optimal order near critical points, J. Comput. Phys. 207 (2005) 542–567.

[24] S. Pirozzoli, Conservative hybrid compact-WENO scheme for shock-turbulence interaction, J. Comput. Phys. 178 (2002) 81–117.

[25] Y. X. Ren, M. Liu, H. X. Zhang, A characteristic-wise hybrid compact-WENO scheme for solving hyperbolic conservation laws, J. Comput. Phys. 192 (2003) 365–386.

[26] D. Kim, J. H. Kwon, A high-order accurate hybrid scheme using a central flux scheme and a WENO scheme for compressible flowfield analysis, J. Comput. Phys. 210 (2005) 554–583.

[27] B. Costa, W. S. Don, Hybrid central-WENO finite difference methods for conservation laws, J. Comput. App. Math.Accepted.

[28] B. Costa, W. S. Don, D. Gottlieb, R. Sendersky, Two-dimensional multi-domain hybrid spectral-WENO methods for conservation laws, Commun. Comput. Phys. 1 (2006) 548–574.

[29] M. R. Meloon, Models of Richtmyer-Meshkov instability in continuously stratified fluids, Ph.D. thesis, California Institute of Technology (1998).

[30] D. J. Hill, C. Pantano, D. I. Pullin, Large-eddy simulation and multiscale modelling of a Richtmyer-Meshkov instability with reshock, J. Fluid Mech. 557 (2006) 29–61.

[31] N. J. Zabusky, A. D. Kotelnikov, Y. Gulak, G. Peng, Amplitude growth rate of a Richtmyer-Meshkov unstable two-dimensional interface to intermediate times, J. Fluid Mech. 475 (2003) 147–162.

[32] G. Peng, N. J. Zabusky, S. Zhang, Vortex-accelerated secondary baroclinic vorticity deposition and late-intermediate time dynamics of a two-dimensional Richtmyer-Meshkov interface, Phys. Fluids 15 (2003) 3730–3744.

[33] J. W. Jacobs, The dynamics of shock accelerated light and heavy gas cylinders, Phys. Fluids A 5 (1993) 2239–2247.

[34] C. E. Niederhaus, Experiments on the Richtmyer-Meshkov Instability of Incompressible Fluids, Ph.D. thesis, University of Arizona (2000).

[35] J. W. Jacobs, V. V. Krivets, Experiments on the late-time development of single-mode richtmyer-meshkov instability, Phys. Fluids 17 (2005) 034104–1–034105–10.

[36] K. O. Mikaelian, Growth rate of the Richtmyer-Meshkov instability at shocked interfaces, Phys. Rev. Lett. 71 (1993) 2903–2906.

[37] D. L. Youngs, Numerical simulation of mixing by Rayleigh-Taylor and Richtmyer-Meshkov instabilities, Laser Part. Beams 12 (1994) 725–750.

[38] D. L. Youngs, Three-dimensional numerical simulations of turbulent mixing by Rayleigh-Taylor instability, Phys. Fluids A 3 (1991) 1312–1320.

[39] A. W. Cook, P. E. Dimotakis, Transition stages of Rayleigh-Taylor instability between miscible fluids, J. Fluid Mech. 443 (2001) 69–99, corrigendum, J. Fluid Mech. **457** (2002), 410.

[40] M. M. Koochesfahani, P. E. Dimotakis, Mixing and chemical reactions in a turbulent liquid mixing layer, J. Fluid Mech. 170 (1986) 83–112.

[41] J. A. Domaradzki, S. Radhakrishnan, Effective eddy viscosities in implicit modeling of decaying high Reynolds number turbulence with and without rotation, Fluid Dyn. Res. 36 (2005) 385–406.

[42] D. C. Wilcox, Turbulence Modeling for CFD, DCW Industries Inc., La Cañada, CA, 1998.

[43] A. R. Miles, B. Blue, M. J. Edwards, J. A. Greenough, J. F. Hansen, H. F. Robey, Transition to turbulence and effect of initial conditions on three-dimensional compressible mixing in planar blast-wave-driven systems, Phys. Plasmas 12 (2005) 056317–1–056317–10.

[44] G. K. Batchelor, The Theory of Homogeneous Turbulence, Cambridge Monographs on Mechanics and Applied Mathematics, Cambridge University Press, New York, 1953.

[45] P. E. Dimotakis, The mixing transition in turbulent flows, J. Fluid Mech. 409 (2000) 69–98.